

REPORT DOCUMENTATION PAGE				Form Approved OMB No. 0704-0188	
<p>The public reporting burden for this collection of information is estimated to average 1 hour per response, including the time for reviewing instructions, searching existing data sources, gathering and maintaining the data needed, and completing and reviewing the collection of information. Send comments regarding this burden estimate or any other aspect of this collection of information, including suggestions for reducing the burden, to Department of Defense, Washington Headquarters Services, Directorate for Information Operations and Reports (0704-0188), 1215 Jefferson Davis Highway, Suite 1204, Arlington, VA 22202-4302. Respondents should be aware that notwithstanding any other provision of law, no person shall be subject to any penalty for failing to comply with a collection of information if it does not display a currently valid OMB control number.</p> <p><b>PLEASE DO NOT RETURN YOUR FORM TO THE ABOVE ADDRESS.</b></p>					
1. REPORT DATE (DD-MM-YYYY) 01-07-2010		2. REPORT TYPE Journal Article		3. DATES COVERED (From - To)	
4. TITLE AND SUBTITLE  Measurement of the Frequency Dependence of the Sound Speed and Attenuation of Seafloor Sands From 1 to 400 kHz				5a. CONTRACT NUMBER	
				5b. GRANT NUMBER	
				5c. PROGRAM ELEMENT NUMBER	
				5d. PROJECT NUMBER	
6. AUTHOR(S)  Michael A. Zimmer, Leonard Dale Bibee, and Michael D. Richardson				5e. TASK NUMBER	
				5f. WORK UNIT NUMBER  74-6639-06	
7. PERFORMING ORGANIZATION NAME(S) AND ADDRESS(ES) Naval Research Laboratory Marine Geoacoustics Division Stennis Space Center, MS 39529				8. PERFORMING ORGANIZATION REPORT NUMBER  NRL/JA/7430-07-6	
9. SPONSORING/MONITORING AGENCY NAME(S) AND ADDRESS(ES)  Office of Naval Research 800 North Quincy Street Arlington VA 22217-5000				10. SPONSOR/MONITOR'S ACRONYM(S)  ONR	
				11. SPONSOR/MONITOR'S REPORT NUMBER(S)	
12. DISTRIBUTION/AVAILABILITY STATEMENT Approved for public release; distribution is unlimited					
13. SUPPLEMENTARY NOTES IEEE Journal of Oceanic Engineering, Vol. 35, No. 3					
14. ABSTRACT  <div style="display: flex; justify-content: space-between;"> <div style="width: 48%;"> <p><i>Abstract</i>—Measurements of sound speed and attenuation were performed over a frequency range from 1 to 400 kHz in the sandy seafloor near Ft. Walton Beach, FL, as part of the 2004 Sediment Acoustics Experiment (SAX04). The measurements at the lowest frequencies, from 1 to 20 kHz, were performed by transmitting tone burst signals from two acoustic sources positioned at depths up to 1 m below the seafloor which were recorded on a 4 m × 4 m array of 35 hydrophones emplaced to depths of between 0.1 and 1 m. Measurements were obtained at frequencies from 40 to</p> </div> <div style="width: 48%;"> <p>200 kHz with the <i>In Situ</i> Sediment Acoustic Measurement System (ISSAMS), a fixed linear array of four piezoelectric probes. The probes were inserted to a depth of 0.3 m, and the outer two probes were used as transmitters, with the inner probes acting as receivers. Sound-speed measurements were also made at 100, 200, and 400 kHz on diver-collected cores using four separate pairs of ultrasonic transducers. The sound-speed measurements above 40 kHz demonstrate an essentially constant sound-speed ratio with frequency of between 1.165 and 1.175, where the sound-speed ratio is the ratio of the speed through the sand to the speed through the</p> </div> </div>					
15. SUBJECT TERMS Attenuation, dispersion, frequency, sand, sound speed					
16. SECURITY CLASSIFICATION OF:			17. LIMITATION OF ABSTRACT  UU	18. NUMBER OF PAGES  20	19a. NAME OF RESPONSIBLE PERSON Dale Bibee
a. REPORT Unclassified	b. ABSTRACT Unclassified	c. THIS PAGE Unclassified			19b. TELEPHONE NUMBER (Include area code) 228-688-5459

# 20100923483

# Measurement of the Frequency Dependence of the Sound Speed and Attenuation of Seafloor Sands From 1 to 400 kHz

Michael A. Zimmer, Leonard Dale Bibee, and Michael D. Richardson

**Abstract**—Measurements of sound speed and attenuation were performed over a frequency range from 1 to 400 kHz in the sandy seafloor near Ft. Walton Beach, FL, as part of the 2004 Sediment Acoustics Experiment (SAX04). The measurements at the lowest frequencies, from 1 to 20 kHz, were performed by transmitting tone burst signals from two acoustic sources positioned at depths up to 1 m below the seafloor which were recorded on a 4 m  $\times$  4 m array of 35 hydrophones emplaced to depths of between 0.1 and 1 m. Measurements were obtained at frequencies from 40 to 200 kHz with the *In Situ* Sediment Acoustic Measurement System (ISSAMS), a fixed linear array of four piezoelectric probes. The probes were inserted to a depth of 0.3 m, and the outer two probes were used as transmitters, with the inner probes acting as receivers. Sound-speed measurements were also made at 100, 200, and 400 kHz on diver-collected cores using four separate pairs of ultrasonic transducers. The sound-speed measurements above 40 kHz demonstrate an essentially constant sound-speed ratio with frequency of between 1.165 and 1.175, where the sound-speed ratio is the ratio of the speed through the sand to the speed through the overlying seawater. The sound-speed ratio determined from the low-frequency array data decreased from 1.135 to 1.115 with decreasing frequency below 20 kHz. Uncertainties in the sound-speed ratio values on the order of  $\pm 0.02$  do not allow meaningful tests of the ability of Biot–Stoll or Buckingham propagation models to describe the observed dispersion. The measured attenuation values show a range from 1 to 120 dB/m with frequency from 1 to 400 kHz. At frequencies above 40 kHz, the attenuation follows a linear trend parallel to the estimates from the Buckingham model, as fit to the data with two free parameters, and at the highest frequencies significantly exceeding the Biot model prediction, as parameterized with values selected from the range of measurements of sediment and pore-water properties made from throughout the SAX04 site. At frequencies below 20 kHz, the data straddle the trends from the two models.

**Index Terms**—Attenuation, dispersion, frequency, sand, sound speed.

Manuscript received April 01, 2007; revised January 23, 2010; accepted June 23, 2010. Date of publication August 16, 2010; date of current version September 01, 2010. The work of M. A. Zimmer was supported by a National Research Council Postdoctoral Fellowship. This work was supported by NRL 6.1 Core Research Program Element 61115N, H. Eppert, Program Manager.

**Guest Editor:** E. Thorsos.

M. A. Zimmer was with the Naval Research Laboratory, Stennis Space Center, MS 39529 USA. He is now with ENSCO, Inc., Springfield, VA 22151 USA (e-mail: zimmer.michael@ensco.com).

L. D. Bibee and M. D. Richardson are with the Naval Research Laboratory, Stennis Space Center, MS 39529 USA (e-mail: dale.bihee@nrlssc.navy.mil; mike.richardson@nrlssc.navy.mil).

Digital Object Identifier 10.1109/JOE.2010.2056230

## I. INTRODUCTION

THE objective of this study was to measure the frequency dependence of the sound speed and attenuation in a homogeneous seafloor sand over a broad frequency range, and to assess the ability of Biot–Stoll and Buckingham propagation models to predict the observed frequency dependences. Due to their effects on the amount of the wave energy reflecting from and penetrating into the seafloor at a given angle of incidence, knowledge of these frequency dependences is critical for reliable detection and imaging of shallowly buried subseafloor objects and for prediction of long-range sonar losses resulting from interactions with the seafloor. While sound-speed and attenuation measurements at high frequency are relatively straightforward, the measurement of their frequency dependence is more difficult due to the limited frequency bandwidth of individual measurement systems. Nevertheless, extrapolation of a single frequency measurement to a broader range of frequencies can be performed if reliable empirical or theoretical relationships have been established to describe the frequency dependences over the desired frequency range.

Biot's model [1], [2] predicts the frequency dependence of sound speed and attenuation due to relative motion between a porous framework and a viscous pore fluid resulting from the deformation and displacement that occur with the passage of small-strain elastic waves. As pore-fluid movement is central to this model, its inputs, as expressed in the Biot–Stoll formulation [3], include a number of descriptors of the pore space, including porosity, permeability, pore size, and tortuosity, as well as the density, bulk modulus, and viscosity of the pore fluid, bulk modulus and density of the sediment grains, and elastic moduli of the dry grain framework. This model predicts significant sound-speed dispersion and a characteristic double power law dependence of attenuation on frequency, where it is proportional to the square of the frequency at low frequency and to the square root of the frequency at high frequency.

The Buckingham model [4], [5] describes the frequency dependence resulting from stochastic stick-slip sliding at grain contacts in a grain framework with no global elastic stiffness. This model requires knowledge of grain and pore fluid properties, as well as inputs that describe the frictional sliding at grain contacts. These parameters cannot be determined from an independent characterization of the sediment, but can be derived from calibration based on measurement of the wave speed and attenuation at a single frequency, or from a fit of the model



to multifrequency measurements. The Buckingham model predicts a weak, approximately logarithmic frequency dependence for the sound speed, and a nearly linear frequency dependence for the attenuation.

Buckingham and Richardson [6] and Williams *et al.* [7] compared sound-speed dispersion and frequency-dependent attenuation measurements made over a frequency range from 0.4 to 400 kHz during the 1999 Sediment Acoustics Experiment (SAX99) near Fort Walton Beach, FL, to Biot model predictions and a Buckingham model fit. Buckingham and Richardson [6], using a subset of the data over a frequency range from 25 to 100 kHz, found that the sound-speed dispersion predicted by the Biot model or fit by the Buckingham model matched the measured dispersion equally well over this bandwidth, whereas the attenuation data were more consistent with the Buckingham model. Williams [7], with the full data set and with inputs from detailed characterization of the seafloor, found that below 50 or 100 kHz the Biot model successfully describes the trend of the observed attenuation and dispersion. Above this frequency, the measured attenuation deviates from that predicted by the Biot model, but follows a trend attributed either to scattering or to the Buckingham sliding mechanisms.

This study, conducted as a component of SAX04 from October 18–30, 2004, involved measuring sound speed and attenuation at frequencies from 1 to 400 kHz in the relatively homogeneous sands in the first meter below the seafloor at a site about 1000 m offshore of Santa Rosa Island near Fort Walton Beach, FL. This frequency range spans from high frequency down through most of the transition to the low-frequency sound-speed minimum predicted by the Biot–Stoll model. A prime focus of the experiment was to make accurate measurements at lower frequencies ( $<20$  kHz), since most of the Biot-predicted dispersion occurs at these low frequencies and there were large measurement uncertainties at these low frequencies in previous studies [7].

## II. SOUND-SPEED AND ATTENUATION MEASUREMENTS AND DATA ANALYSIS

Three separate measurement systems were used to measure the sound speed and attenuation over a frequency range from 1 to 400 kHz. These systems included a core measurement system for measurements from 60 to 400 kHz, a four-probe piezoelectric array for frequencies from 15 to 200 kHz, and a diver-emplaced hydrophone array for frequencies below 20 kHz. Waveforms recorded with each of the three measurement systems were processed to calculate values of sound speed and attenuation at several frequencies within the frequency range of each system.

The hydrophone array was emplaced approximately 200 m to the north–west of the *R/V Seward Johnson*, at  $30^{\circ} 23.283' \text{ N}$ ,  $86^{\circ} 38.671' \text{ W}$ , at a water depth of 17 m. The cores were collected in the immediate vicinity of the array. The piezoelectric array was deployed at three locations within 25 m north of the *R/V Seward Johnson*. Sediments from three vibracores collected in April 2006 near the site of the array consisted of a clean, well-sorted, quartz sand with sporadic shells and thin mud lenses within the upper 5 m of sediment.

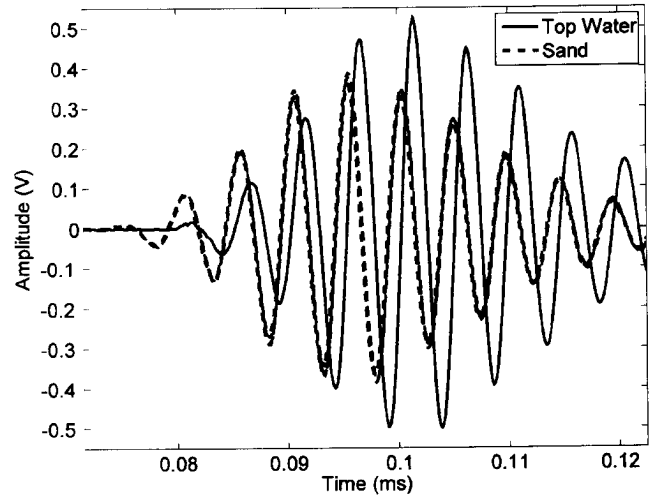


Fig. 1. Sample waveforms taken at 5-cm intervals down the core with the 200-kHz transducers. The four traces through the sand all roughly overlie one another.

### A. 60–400 kHz: Core Measurements

Sediment cores were collected by pushing a 5.9-cm diameter core tube by hand vertically down into the seabed, then capping the top of the tube and digging down around the core tube to cap the bottom of the tube. Careful handling of the cores during and after collection reduced the effects of disturbance on sediment structure. The divers collected five sediment cores, each approximately 25 cm long, from the site of the hydrophone array. The cores were brought shipboard and stored until sound-speed and attenuation measurements were made three days after their collection. Sound-speed and attenuation measurements were made on each of these cores using four separate pairs of transducers with resonance frequencies of 60, 100, 200, and 400 kHz. Each pair of transducers, with fixed separation distances, was placed on either side of the core tube. The transmitting transducer was driven with five cycles at the resonance frequency and the waveform received by the other transducer was recorded with a digital oscilloscope at sample rates of 2.5, 5, 10, and 25 MHz for the four respective frequencies. For each set of transducers, signals were recorded at 5-cm intervals below the sediment–water interface, as well as through the water in the core tube overlying the sediment. Fig. 1 shows example waveforms collected for one of the cores at 200 kHz.

The sound speed through the sediment in each core was calculated by cross correlating the time series through the sand with that collected through the top water of that core. This was accomplished by removing the direct current (dc) offset from each time series and upsampling each at 100 times the original sample rate by spectral interpolation to increase the resolution of the cross correlation. The time series was windowed over the first four cycles to reduce the increased impact of multipath in the later cycles, then cross correlated with the signal through the top water. The sound-speed ratio, or the ratio of the sound speed through the sediment  $c$  to the sound speed through the overlying

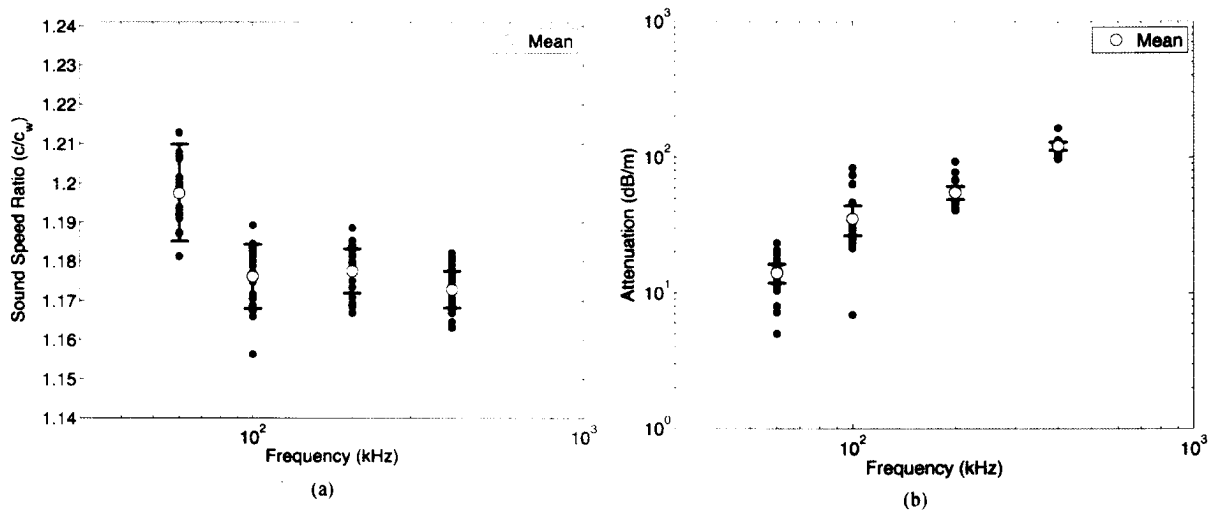


Fig. 2. Results from the core measurements: (a) sound-speed ratio and (b) attenuation plotted against frequency. Each black point represents the value derived from an individual measurement. The open point shows the mean value, with the error bars showing its 95% uncertainty limits.

water  $c_w$ , was calculated from the time lag between the two signals  $t_{lag}$ , the water speed  $c_w$ , and the inner diameter of the core tube  $d$ , according to

$$\frac{c}{c_w} = \frac{1}{1 - \left( \frac{c_w t_{lag}}{d} \right)} \quad (1)$$

and presented in Fig. 2(a). The water speed was estimated to be 1526 m/s from the salinity measured with a conductivity–temperature–depth (CTD) device at the seafloor on the day that the cores were collected and the water temperature measured in the core at the time of the sound-speed measurements. The attenuation  $\alpha$  was calculated as

$$\alpha = \frac{20 \log_{10} \left( \frac{A_w}{A} \right)}{d} \quad (2)$$

where  $A$  and  $A_w$  are respectively the root mean square (rms) magnitudes of the windowed segments of the sediment and overlying water signals, assuming negligible attenuation in the water [Fig. 2(b)].

The uncertainty in each data point of the sound-speed ratio was estimated by assuming uncertainties in the water speed of 0.32 m/s [8] and in the core diameter of 2%, based on measurements of the variability in the inner diameters of the core tubes used to collect the cores, and by performing a bootstrap analysis to estimate the uncertainty in the time lags, as described in Appendix I. The errors were then combined using standard error propagation techniques through (1). The errors in the attenuation were calculated by estimating the uncertainty in the amplitude ratio from the bootstrap analysis described in Appendix I and assuming a 2% error in the diameter, then propagating the errors through (2). The 95% confidence intervals of the mean values at each frequency are shown by the solid lines. The uncertainties in the mean values at each frequency were calculated as the square root of the sum of squares of the uncertainties in

the individual measurement values and two standard deviations of the values around the mean divided by the square root of the number of samples.

We attribute the larger sound-speed ratio values at 60 kHz relative to those observed at the higher frequencies to be a systematic error resulting from the short travel distance in the sediment (5.9 cm) relative to the acoustic wavelength at that frequency ( $\sim 3$  cm). A similar though somewhat smaller rise in the sound speed at this frequency is found when calculating the sound speed in the top water when referenced to a distilled water sample. For this reason, both the sound-speed and attenuation data at 60 kHz are removed when performing the data-model comparisons below.

#### B. 15–200 kHz: *In Situ* Sediment Acoustic Measurement System

The *In Situ* Sediment Acoustic Measurement System (IS-SAMS) consists of two linear, four-probe piezoelectric arrays, mounted rigidly on a diver-emplaced frame at a spacing of 30 cm [Fig. 3(a)]. Each probe contains a piezoelectric element encased in the tip of the probe; the cylindrical probes contain compressional elements, while the paddle-shaped probes contain shear elements. The shear wave data were not used as part of this study. The probes all extend 30 cm below the base of the frame. The system is placed onto the seafloor and the probes are driven down into the seabed until the base of the frame rests on the seafloor. Each of the two outer compressional probes was driven with tone bursts of between 5 and 25 cycles at frequencies of 15–200 kHz. The output of each of the inner probes on the compressional array was digitized at a 2.5-MHz sample rate with a high-speed digital recording system, averaged ten times, and the average time series recorded.

The difference in the distance between each transmitter and the two receivers was calculated from the water sound speed and from the average time delay calculated by cross correlation of calibration signals recorded at the two receivers collected while the system was suspended in the water column. This calculated distance, plotted against frequency in Fig. 3(b), was used in lieu

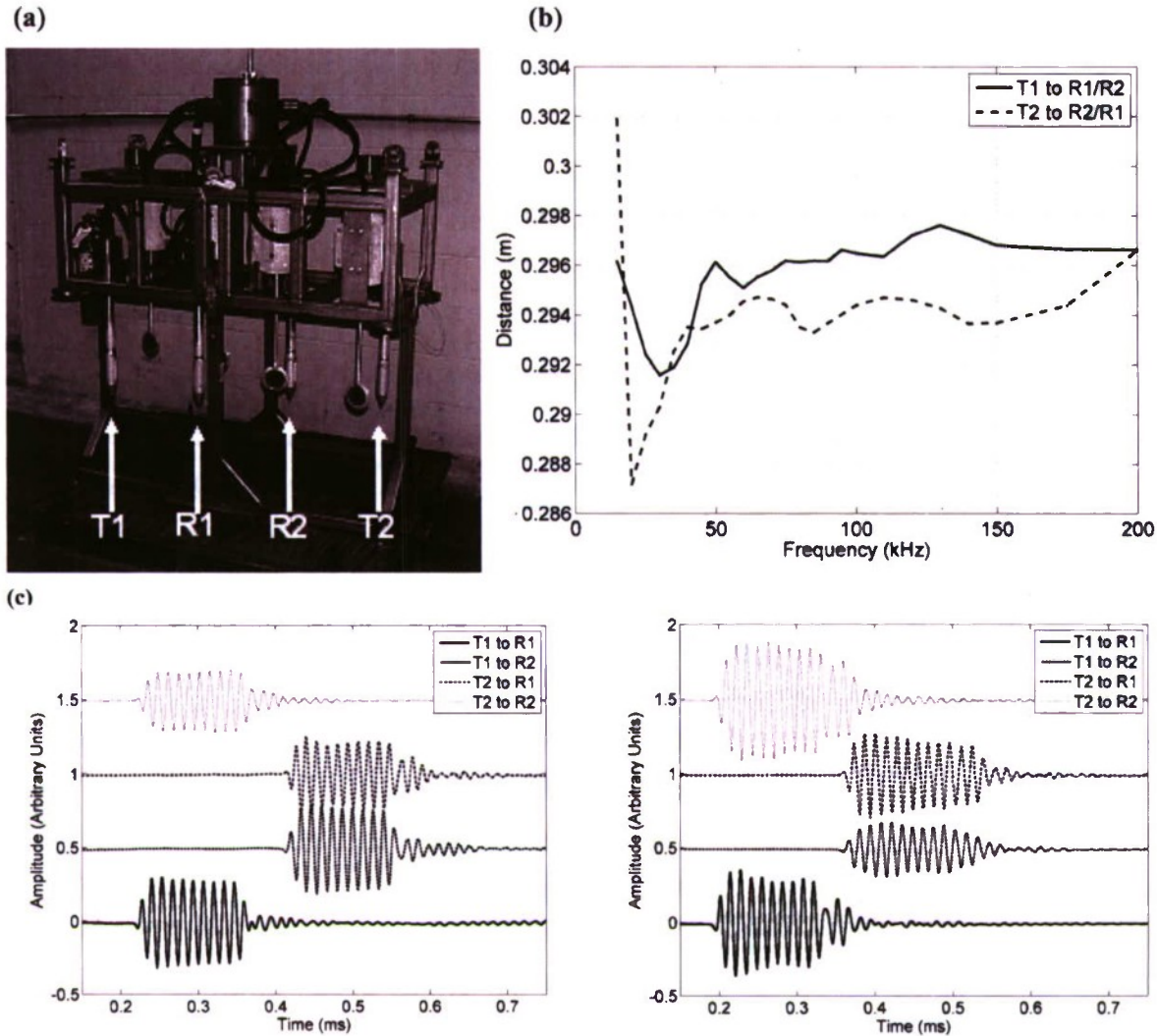


Fig. 3. (a) Photograph of the ISSAMS system on its stand with compressional probes labeled; (b) effective difference in transmitter-receiver distance versus frequency; (c) raw sample waveforms at 75 kHz collected with the instrument suspended in the water column; (d) raw sample waveforms at 75 kHz collected with the instrument implanted in the seabed.

of the physically measured distance to account for effects such as the transducer element's effective center not being located at the center of the probe or not being located in the same location for signals approaching from opposite sides of the probe. The large deviation in the values below 40 kHz relative to the high-frequency trend suggests that some form of interference, such as multipath or resonance in the apparatus, is affecting the travel times derived from the water-calibration signals at lower frequencies. The average distance calculated using the values from only frequencies above 40 kHz was therefore used as the effective difference in the transmitter-receiver distance at all frequencies. Raw sample time series from each source-receiver pair at 75 kHz are shown as collected with the apparatus suspended in the water column in Fig. 3(c) and with the apparatus implanted in the seafloor in Fig. 3(d).

The sound speed at each frequency was calculated by first filtering each time series to a band 0.75–1.25 times the center frequency of the tone burst. Each signal was then upsampled by a factor of 100 with spectral interpolation and windowed to a number of cycles equal to the number of drive cycles. The

signals recorded on the two receivers from the same transmitter were cross correlated to determine the difference in the travel time from the transmitter to the two receivers. The sound-speed ratio was then calculated from (1), with the distance  $d$ , in this case being the effective difference in the distance from the transmitter to each of the receivers. The attenuation was calculated from the ISSAMS measurements by the transposition method, which uses the signal magnitudes from all four probes to remove coupling and receiver sensitivity effects in the magnitude values [9]. The attenuation  $\alpha$  in decibels per meter was calculated from the distances between the transducers  $d_{T1,R1}$ ,  $d_{R1,R2}$ , and  $d_{R2,T2}$  and the peak magnitudes of the signals recorded between each source and receiver pair  $A_{T1,R1}$ ,  $A_{T1,R2}$ ,  $A_{T2,R1}$ , and  $A_{T2,R2}$  according to

$$\alpha = \frac{4.343}{d_{R1,R2}} \ln \left[ \frac{d_{T1,R1}}{d_{R1,R2} + d_{T1,R1}} \times \frac{d_{R2,T2}}{d_{R1,R2} + d_{R2,T2}} \times \frac{A_{T1,R1}}{A_{T2,R1}} \times \frac{A_{T2,R2}}{A_{T1,R2}} \right]. \quad (3)$$



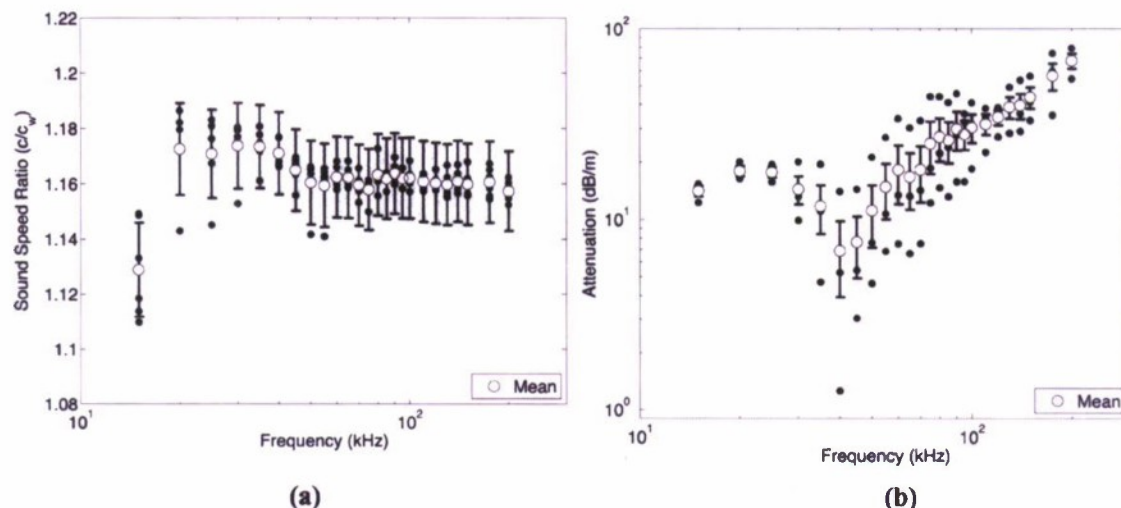


Fig. 4. Results from the ISSAMS measurements: (a) sound-speed ratio and (b) attenuation plotted against frequency.

The sound-speed ratio and attenuation derived from the ISSAMS data are plotted against frequency in Fig. 4. The individual black points at each frequency represent the values derived from measurements made at the three locations at which the apparatus was deployed, with two sound-speed points being generated at each location using the data from the two transmit probes. The open points in Fig. 4 represent the mean value of the measurements at each frequency. The uncertainty for each value was estimated in a similar fashion as for the core data. The uncertainties in the time lags and in the amplitude ratio were generated by a bootstrap analysis as described in Appendix I. The uncertainty in the distance was taken as the standard deviation in the effective distances calculated from the calibration signals at frequencies above 40 kHz. As for the core results, the uncertainties for the ISSAMS results are dominated by the uncertainty in the distance between the transducers. The solid lines represent the 95% confidence intervals of the mean values, calculated as for the core values as a combination of the individual sample uncertainties and the standard deviation of the values around the mean divided by the square root of the number of samples. The anomalous rise in the sound-speed ratio and attenuation below 40 kHz corresponds to the drop in the effective distance measured from the calibration signals at those frequencies [Fig. 3(b)], suggesting that whatever interference effects are affecting the time lags in the calibration data continue to impact the time lags once the apparatus is implanted into the seafloor. For this reason, the data below 40 kHz are removed from the data-model comparisons below.

### C. 1–20 kHz: Buried Hydrophone Array

The low-frequency acquisition system was designed to allow measurements of sound speed and attenuation in shallow seafloor sands at frequencies from 1 to 20 kHz. The system used a subseafloor receiver array to record signals propagating laterally through the seafloor sediments, generated by acoustic sources placed on or implanted up to 1 m below the seafloor around the receiver array. The array geometry was designed based on full waveform simulations conducted with the Ocean

Acoustics and Seismic Exploration Synthesis (OASES) modeling package [10] to reduce the interference from multipath signals on sound-speed and attenuation measurements. These simulations indicated that waterborne signal paths would generate significant interference to the sediment-borne signals when the source and receivers were both located either at or above the seafloor. The models predicted that significant interference from the waterborne signals would persist when both the source and receivers were buried below the seafloor to depths of approximately 25 cm, with diminishing waterborne signal strength continuing below that depth. When both the source and receivers are buried, reflections of the acoustic signals off the overlying sediment–water interface also produce interference. More deeply buried array elements increase the separation between direct path and seafloor-reflected arrivals, but also increase the risk of interference from signals reflected off or refracted through deeper sediment layers, which were thought to be present as shallow as 1 m below the seafloor. To allow as much separation as possible from the seafloor as well as from potential subseafloor sediment interfaces, the receiver array was designed to include receivers buried at depths from 0.1 to 1 m. Likewise, the sources were placed on the seabed and buried to depths of up to 1 m.

The receiver array consisted of 35 hydrophones and five three-component accelerometers. The hydrophones all consist of a piezoelectric element attached to a small preamp and potted in polyurethane, resulting in a package 2.54 cm in diameter and 11.4 cm in length, as shown on the right-hand side of Fig. 5(a). Each three-component accelerometer consists of three high sensitivity, uniaxial piezoelectric accelerometers, mounted orthogonally in an aluminum pressure case 7 cm in diameter and 12.7 cm in length, shown on the left-hand side of Fig. 5(a). Divers implanted the receivers at depths of between 0.1 and 1 m below the seafloor along three azimuths within a 4 m × 4 m area (Fig. 6) using a positioning template consisting of an aluminum frame with guide tubes mounted at each of the receiver locations [Fig. 5(b)]. Water-jet tools used to embed the two types of receivers into the seabed were designed to fit tightly into the guide tubes on the frame to ensure precise location of

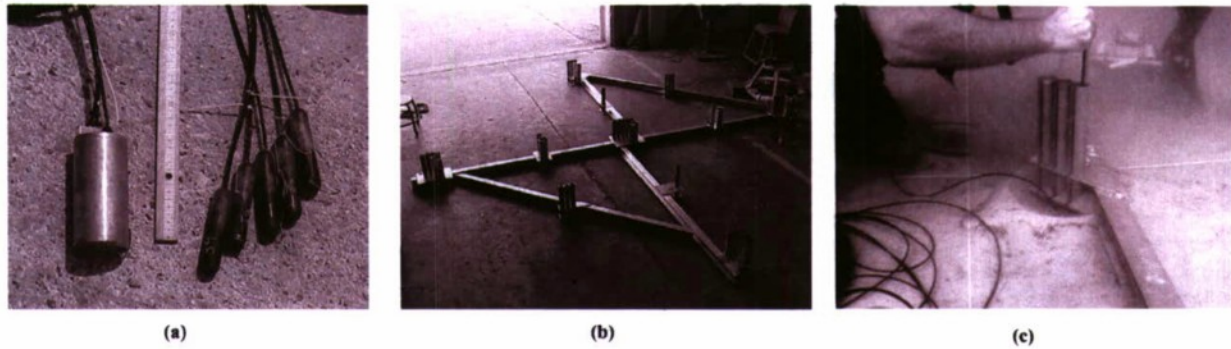


Fig. 5. (a) Photograph of a three-component geophone (left) and a set of five hydrophones (right), with a meter stick with 1-cm markings for scale; (b) photograph of the receiver positioning template; and (c) photograph of the divers water jetting a hydrophone into the seabed.

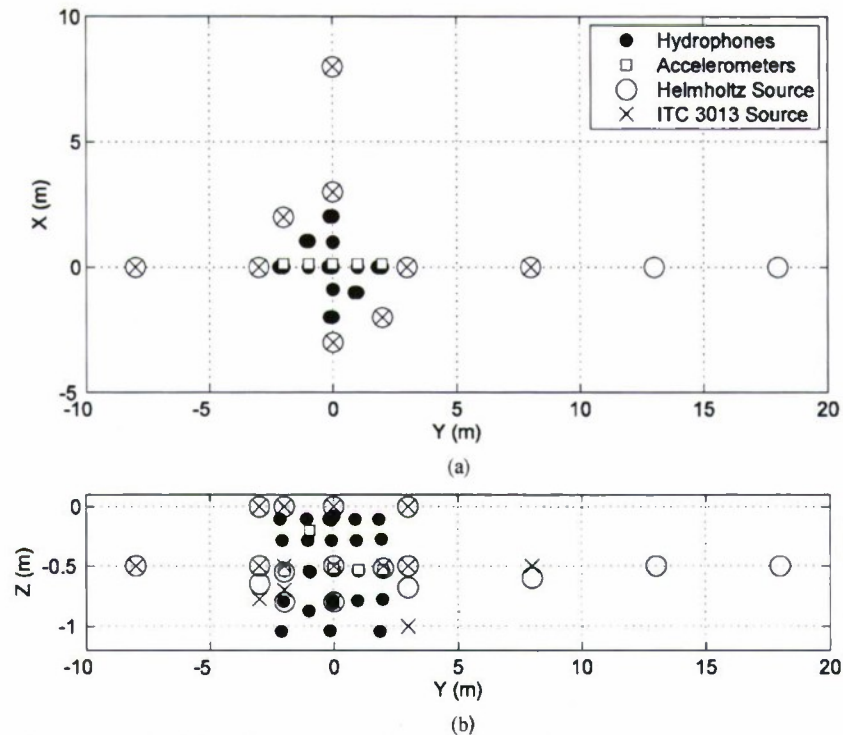


Fig. 6. Map of source and receiver positions for the low frequency array: (a) map view and (b) side view.

each receiver, both laterally and vertically. Field modifications of the water-jet tools were required as sand collecting within the tools prevented the receivers from being released by the tools. These modifications resulted in the placement tools being much smaller than the guide tubes on the template [Fig. 5(c)], leading to inaccuracies of up to 5 cm in the positions of the receivers from the intended location. The craters in the seabed that were formed on insertion of each sensor as seen in Fig. 5(c) were left to be filled in by wave action. Each sensor was connected to a data acquisition unit located in a seafloor pressure container, where the signals from each receiver were amplified and filtered, then digitized with 24-b resolution at a sampling frequency of 102.4 kHz and stored on a PXI computer. The data were retrieved from the seabed computer via a fiber optic cable.

This array was used to record signals from two acoustic sources positioned on or below the seabed off each axis of the array. The sources, a Helmholtz generator [Fig. 7(a)] driven at frequencies from 1 to 6 kHz, and an ITC 3013 hemispherical transducer [Fig. 7(b)] driven at 6–20 kHz, were all positioned

at points along each of the main azimuths of the receiver array at distances from 3 to 18 m from the center of the array (Fig. 6). At most source locations, sources were water jetted to a depth of 50 cm below the seafloor, though at the positions nearest to the array they were also placed at the seafloor and at depths of approximately 1 m below the seafloor. The sources were all driven with ten cycle tone bursts at each frequency. The signals recorded on each receiver were averaged ten times if the divers were waiting to move or swap out sources, or 100 times when the source was being left in place overnight, and recorded on the seabed computer. Fig. 8 shows representative signals from each source when positioned in close proximity to the array. High-quality signals were recorded at all but the highest frequencies (above 15 kHz), at which the system noise began to be significant relative to the strength of the signal at the farthest receivers. The data from the accelerometers showed long ring times due to resonances within the accelerometer housings and could not be used.



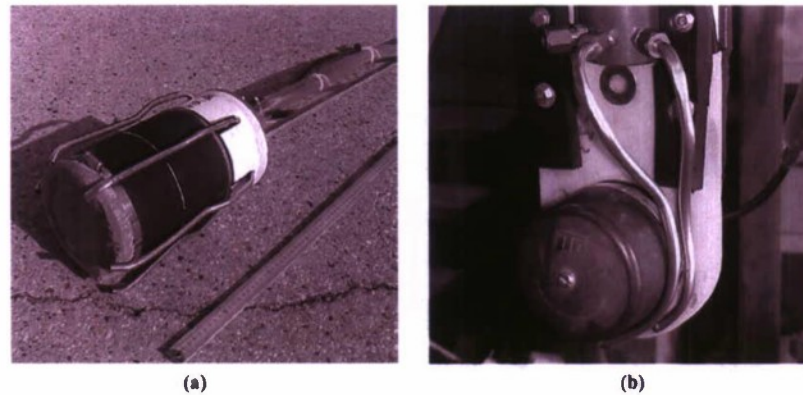


Fig. 7. Photographs of the two acoustic sources: (a) the Helmholtz generator and (b) an ITC 3013 hemispherical transducer.

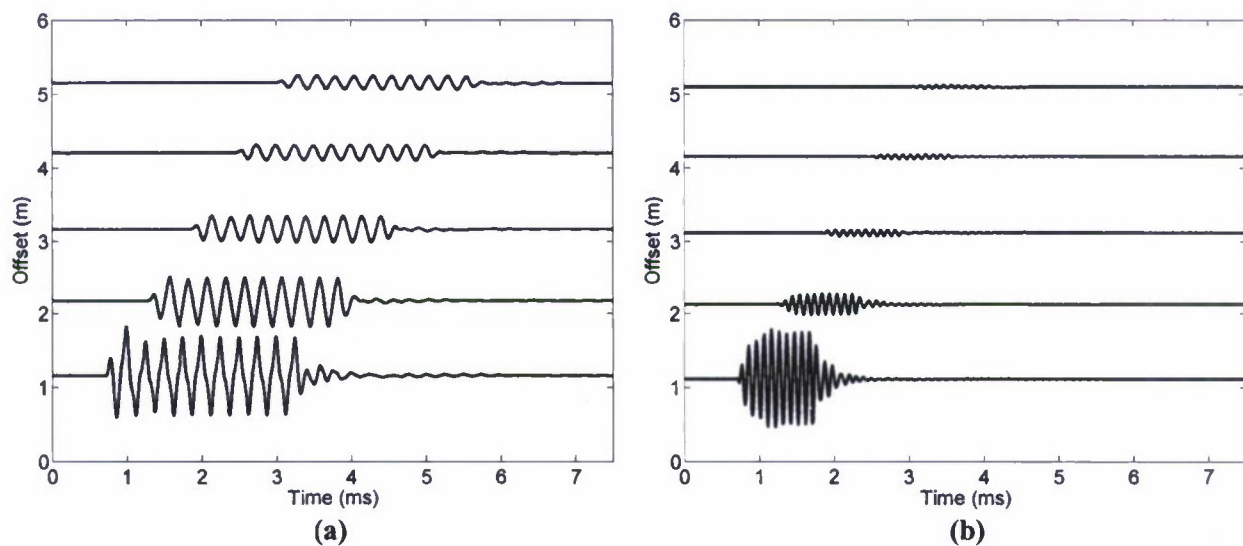


Fig. 8. Representative time series from the hydrophones at 50-cm depth along the center of the array (0,  $-2$  to  $2$ ,  $-0.5$ ) with the source at a depth of 50 cm positioned 1 m off the end of the array (0,  $-3$ ,  $-0.5$ ): (a) 4 kHz and (b) 10 kHz.

Two separate analyses of the sound speed and attenuation from the low-frequency array data were performed in an effort to isolate the direct path signals from the multipath signals. The first analysis involved deconvolving each trace with the source wavelet and calculating sound speed and attenuation from the arrival times and magnitudes of the appropriate peak of the deconvolved waveforms. The second analysis consisted of a full waveform inversion for the sound speed and attenuation from the time series recorded at all 35 receivers for a single source location using the OASES model as a forward model.

The deconvolution analysis was performed by deconvolving each data trace with a source wavelet derived from the signal recorded at the nearest hydrophone to the source when placed 1 m off the south end of the array at a depth of 50 cm, e.g., the bottommost traces in Fig. 8. The source wavelet for each frequency was generated by windowing the time series from this source–receiver pair to remove later arrivals, then deconvolving it with an impulse time series to remove interference from the seafloor reflection. The impulse time series consisted of a unit magnitude spike at the estimated arrival time of the

direct path signal and a second spike at the estimated time of the seafloor-reflected arrival, with its magnitude scaled by the reflection loss calculated from the Zoeppritz equations [11], which assume a planar interface between two elastic layers, and by the spreading loss of the reflected path length relative to the direct path length. As the source and receiver locations and the sound speeds used to estimate the times of the two arrivals were approximate, the arrival time and magnitude of the seafloor reflection in the impulse time series was manually adjusted to produce consistent peak heights throughout the resultant source wavelet, as observed in the waveforms collected during calibration tests with both the source and the receiver suspended in water. The calibration waveforms themselves were not used to generate the source wavelets as they differed significantly from the wavelets observed at the buried receivers, likely because of the effect of the sediment loading the source once it was placed on or buried in the seafloor. The deconvolved source wavelet  $u$  was calculated by dividing the Fourier transform of the impulse time series  $F(a)$  into the Fourier transform of the data trace from that source–receiver



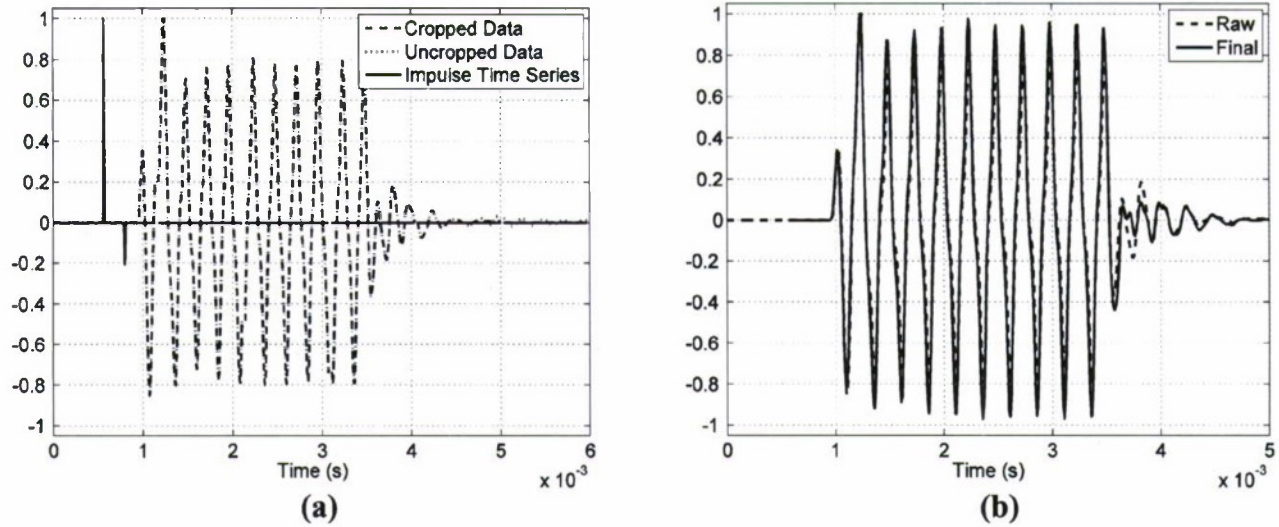


Fig. 9. Example at 4 kHz of the process used to generate the source wavelets showing (a) the raw and cropped data and impulse time series and (b) the raw time series and resultant source wavelet. The ordinates of each plot are the amplitude scaled to a maximum value of 1.

pair  $F(r_a)$ , then performing the inverse Fourier transform according to

$$u = F^{-1} \left( \frac{F(r_a)}{F(a)} \right). \quad (4)$$

An example of the process used to generate the source wavelets is shown in Fig. 9.

Once the source wavelets had been generated, the deconvolution was performed by dividing the Fourier transform of the source wavelet  $F(u)$  into a Blackman–Harris window  $w$  that was between 0.4–1.6 and 0.05–1.95 times the drive frequency. The resulting deconvolution operator was then multiplied by the Fourier transform of each data trace  $F(r)$  to generate the frequency-domain representation of the deconvolved waveform, with the magnitude spectrum of the deconvolved wavelet approximately equal to the Blackman–Harris window. The larger relative window bandwidths were used at the lower frequencies to increase resolution to allow better separation of the peaks corresponding to the direct path and interference paths in the deconvolved time series at low frequency. The inverse Fourier transform was then performed to produce the deconvolved time series  $r_d$  according to

$$r_d = F^{-1} \left( \frac{w}{F(u)} F(r) \right) \quad (5)$$

replacing the source signals in the time series with peaks centered on the arrival time of each arriving signal, with one or more small side lobes on either side of each peak, and with the height of each peak being proportional to the pressure amplitude of each arriving signal.

Raw data traces and corresponding deconvolved traces for four combinations of source and receiver depths are shown in Figs. 10 and 11 for frequencies of 4 and 10 kHz, respectively. When the source is placed on the seabed, each of the receivers records the direct arrival as well as evanescent wave energy and scattered arrivals that travel over most of their path at the sound

speed of the water just above the seabed before propagating down into the seafloor. The shallower hydrophones are dominated by this water path energy [see Figs. 10(a) and 11(a)], whereas deeper receivers [Figs. 10(b) and 11(b)] demonstrate smaller, but still noticeable, water path arrivals, especially at the farther receivers. When the source is embedded below the seafloor, weak water-speed arrivals are still visible on some traces: e.g., the top most two traces in the right panel of Fig. 10(c)–(d) show the influence of water path arrivals. While these arrivals are not explainable by reflection or refraction from a high to low impedance interface, full waveform modeling does clearly demonstrate the presence of this class of arrivals from sources and receivers at these depths. When both the source and receivers are embedded below the seafloor, the energy in these waterborne arrivals is minimized, though in this configuration the strength of the reflection off the seafloor can be significant, e.g., a reflected arrival is clearly visible in the lowermost trace on the right-hand side panel of Fig. 11(d). Additional arrivals from energy reflected or scattered off sub-seafloor sedimentary layers or heterogeneities can also be seen in many traces.

The time and height of the peak corresponding to the direct arrival in each deconvolved time series were taken as the arrival time and relative pressure magnitude for each trace. To reduce the impact of arrivals other than direct arrivals on the sound speed and attenuation, peaks picked for each of the > 10 000 deconvolved traces were each manually verified to remove traces where there was ambiguity in which peak corresponded to the direct arrival. Traces where the direct arrival peak was not at least twice as large as neighboring peaks were excluded from later analysis. Even after this quality check, the impact of multipath interference on the arrival times and pressure magnitudes can be seen in the remaining data. Fig. 12 shows the arrival time and pressure magnitude from each trace collected at 4 and 10 kHz plotted against the source–receiver distance. The arrival times shown in the figure have been reduced by the source–receiver distance ( $d$ ) divided by 1750 m/s to allow separation of

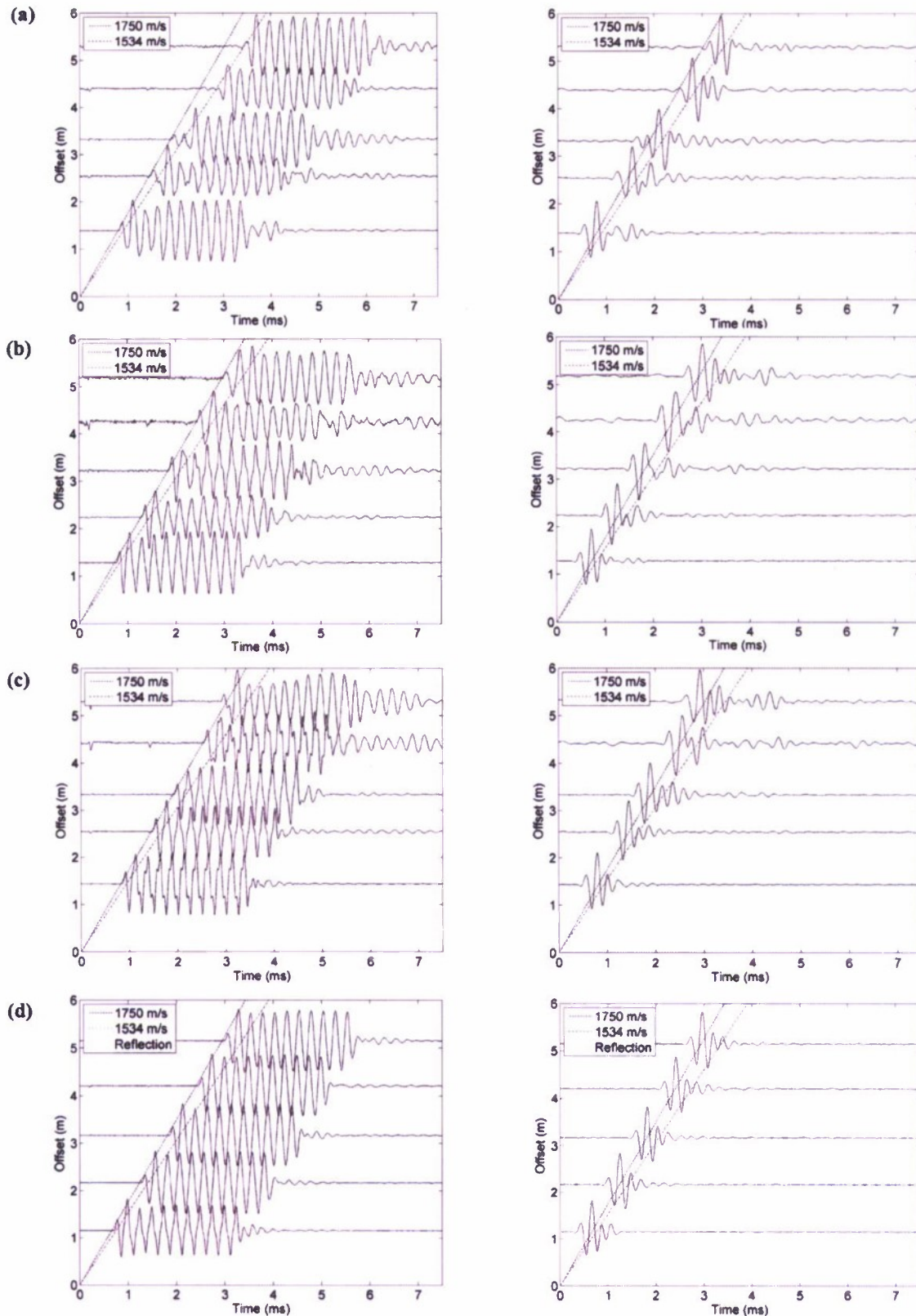


Fig. 10. Time series data (left) and deconvolved traces (right) at 4 kHz: (a) receivers at  $\sim 10$ -cm depth and seabed source, (b) receivers at 50-cm depth and seabed source, (c) receivers at  $\sim 10$ -cm and the source at 50-cm depth, and (d) receivers and source at 50-cm depth. Each trace is scaled to a maximum amplitude of 1.

the data. The reduced times do not trend to zero due to a constant offset time resulting from the approximate location of the spike for the direct arrival in the impulse time series when gen-

erating the source wavelet used in the deconvolution. The difference between the arrival times of the data where either the source or the receiver was at depths less than 25 cm and of that



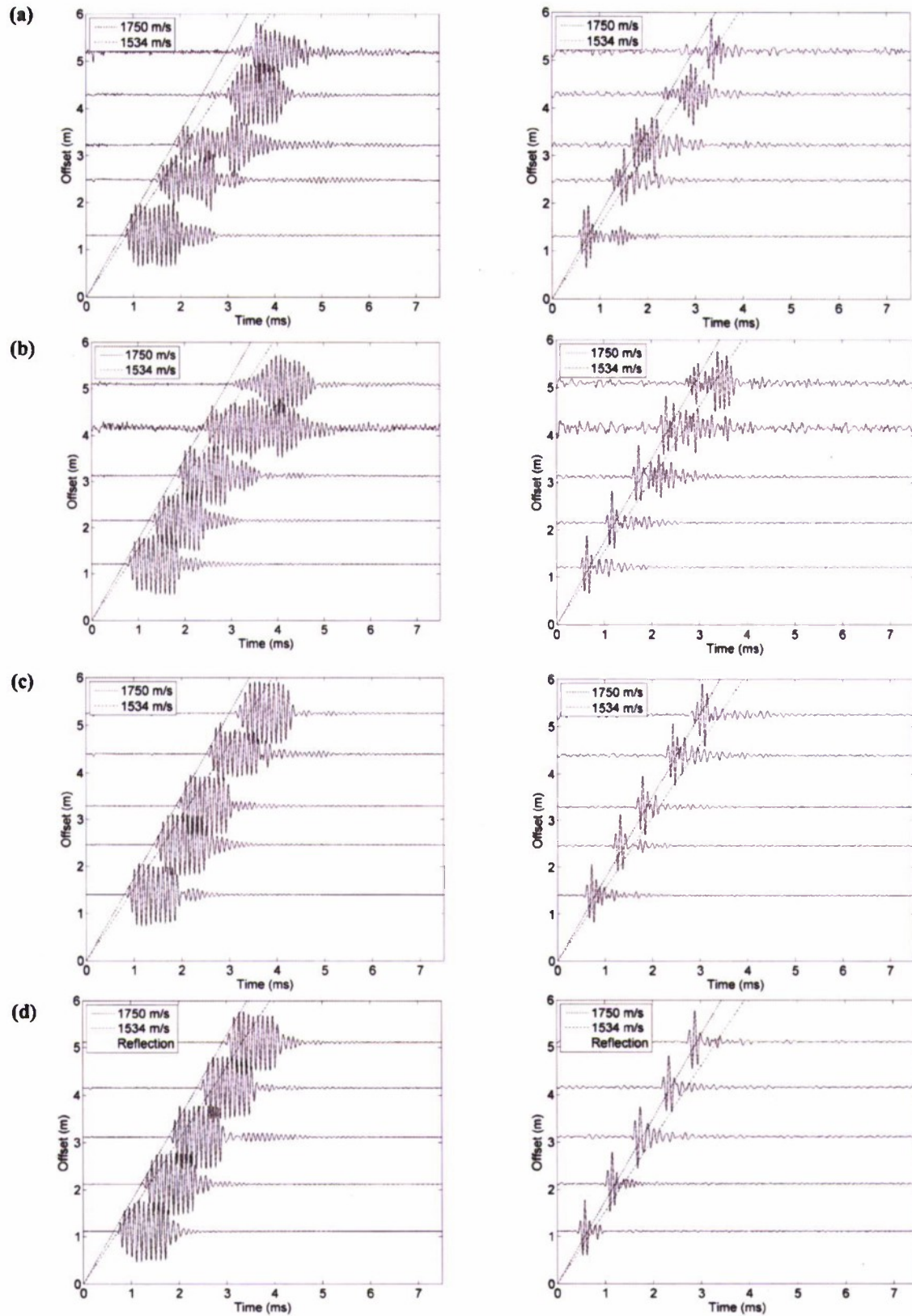


Fig. 11. Time series data (left) and deconvolved traces (right) at 10 kHz: (a) receivers at  $\sim 10$ -cm depth and seabed source, (b) receivers at 50-cm depth and seabed source, (c) receivers at  $\sim 10$ -cm and the source at 50-cm depth, and (d) receivers and source at 50-cm depth. Each trace is scaled to a maximum amplitude of 1.

where both were deeper than 25 cm is relatively limited at these frequencies; the shallower data have slightly more scatter. On the contrary, the magnitudes demonstrate a significant separa-

tion between data from shallow sources or receivers and data from deeper sources and receivers (right-hand side frames of Fig. 12), with shallower data demonstrating lower magnitudes.

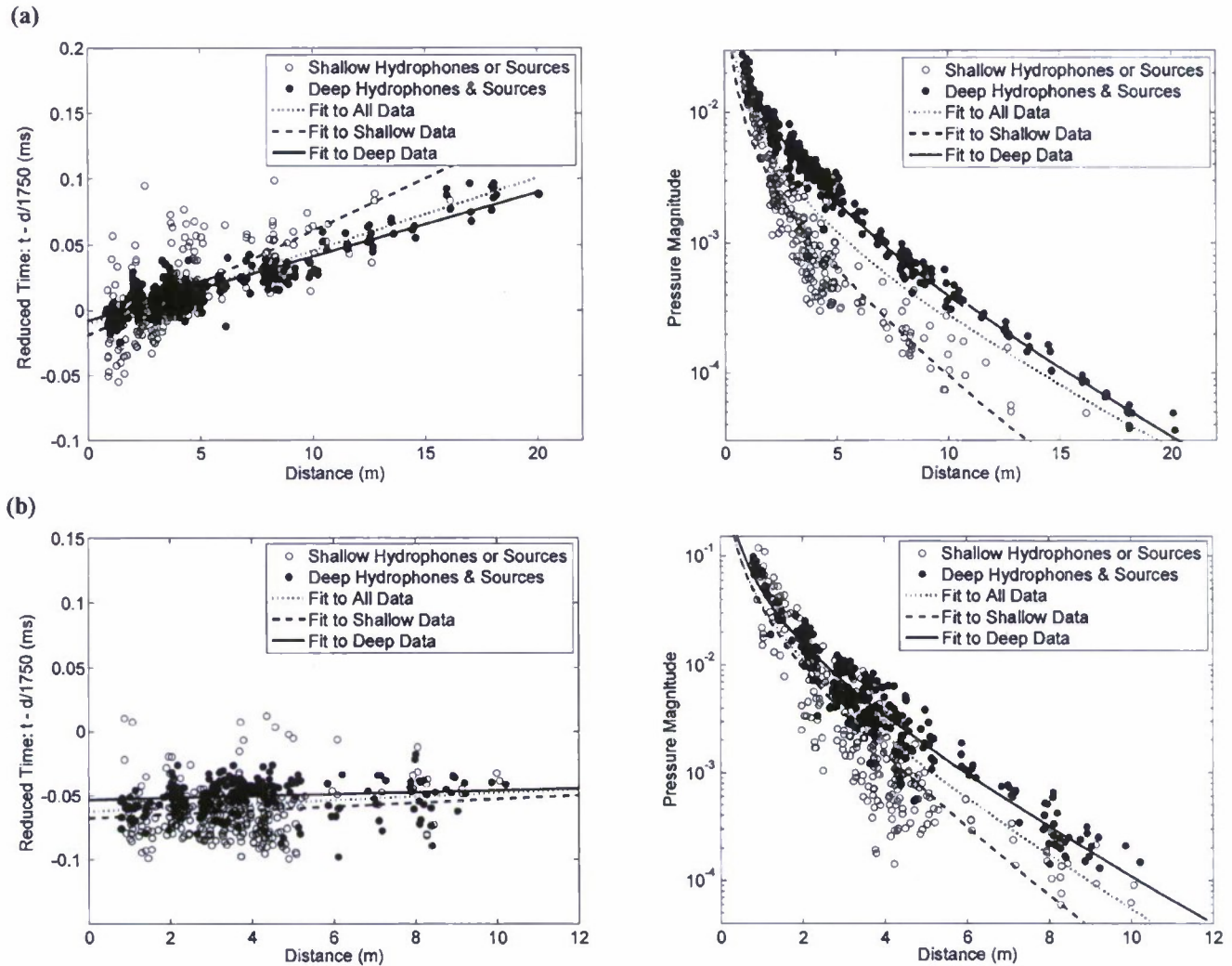


Fig. 12. Reduced arrival times (left) and pressure magnitudes (right) for the data at (a) 4 kHz and (b) 10 kHz.

Values of sound speed were calculated for each frequency from a linear least squares fit to the arrival time versus the source–receiver distance. Similarly, values of attenuation were calculated from a linear least square fit of the log of the peak magnitudes of the deconvolved traces, corrected for spherical spreading, to the source–receiver distance. To mitigate uncertainty in the placement of array elements, arrival times picked from the deconvolution peaks at select frequencies were used to invert for the source and receiver positions before calculating the sound speed and attenuation. This inversion was performed by first holding the receiver positions fixed and performing a linearized, iterative inversion of the arrival times for the source positions of each of the sources, as described in Appendix II. For the Helmholtz resonator, the inversions used only data collected at 5 and 6 kHz as these frequencies demonstrated the highest resolution among the data collected with that source, ensuring the best separation of interfering arrivals. The inversion for the locations of the ITC 3013 source used only the 10- and 12-kHz data, as these data had the highest signal-to-noise ratio of the data collected with the higher frequency source. The source positions were then held fixed and the same sets of arrival times were used to invert for the receiver positions

in an analogous manner as for the source positions. The positions inverted at each frequency were averaged to estimate the locations of each receiver and source position. Error analysis of the average positions, as described in Appendix II, yielded 95% confidence limits of 5 cm for the receivers, of 7 cm for the ITC 3013 source, and of 12 cm for the Helmholtz resonator source. As sound speed is a free parameter in the inversion, the inversion for the source and receiver positions can result in a systematic error in values of the sound speed and attenuation. Nevertheless, the inversion will reduce random errors associated with array element location inaccuracies, allowing a clearer observation of the magnitude of the dispersion. The systematic error due to array element location uncertainties is also included in the calculation of confidence intervals for the sound speed and attenuation.

Fig. 13 shows the sound-speed ratios and attenuations calculated from fits to arrival times and magnitude data from the entire data set as well as to subsets consisting of data from just the shallow sources or receivers and from just the deeper sources and receivers. The error bars in Fig. 13 represent 95% confidence intervals that include the uncertainty in the least squares fit as well as the uncertainty in receiver positions over the length



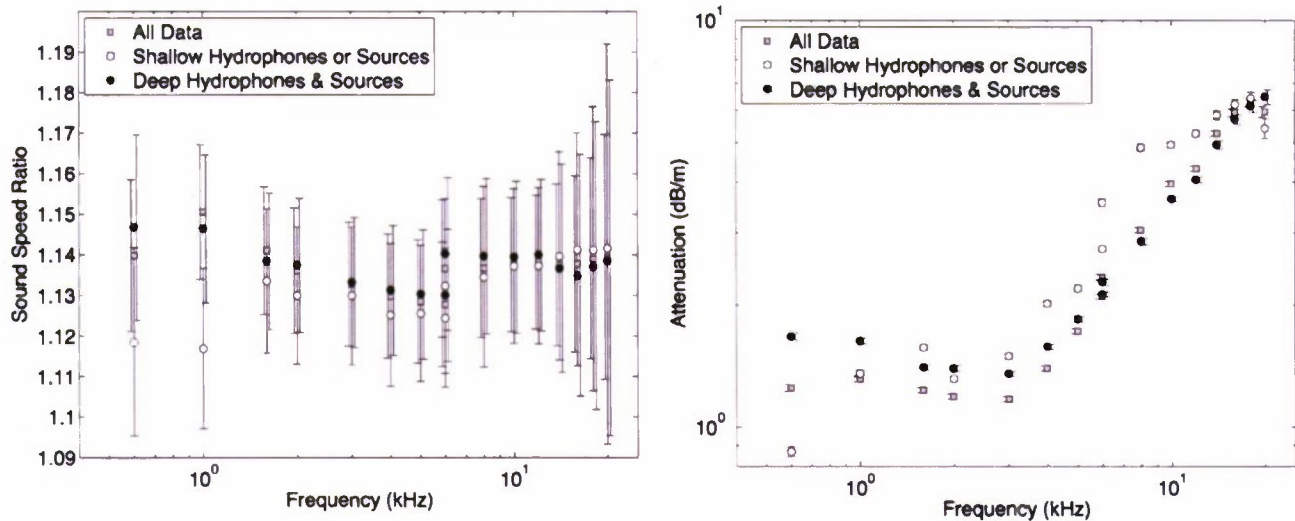


Fig. 13. Sound-speed and attenuation results from the deconvolution analysis of the low-frequency array data. The error bars for the results from the entire data set are shifted slightly to the left, and those from the deep array elements to the right, while those from the shallow elements are in the center on each point.

of the array (1.2%). At all but the lowest frequencies, values of the sound speed and attenuation from the shallow or deep subsets are consistent with those from the full data set, relative to the overall variation with frequency. The results demonstrate an essentially constant sound speed for data collected with the ITC 3013 source from 6 to 20 kHz. The offset at 6 kHz between values from the two different sources suggests systematic errors likely due to positioning inaccuracy of the sources. Below 4 kHz, values of the sound-speed ratio increase consistently for all three sets of data by approximately 0.02 until 1.5 kHz, below which values of the sound-speed ratio from the separate subsets diverge. Values of attenuation demonstrate a consistent decrease with decreasing frequency down to 3 kHz, below which values of attenuation rise slightly. These increases in sound speed and attenuation at low frequency suggest systematic errors due to the influence of nondirect arrivals on the data analysis.

To assess the impact of nondirect arrivals on the sound speed and attenuation derived from our analysis, the same deconvolution-based analysis was applied to a simulated data set generated by a full waveform model (OASES) for a setting similar to that in which the actual data were collected. The model consisted of an elastic half-space with a sound speed of 1750 m/s, with no frequency dispersion, and with attenuation of 1.0 dB/ $\lambda$ , density of 2051 kg/m<sup>3</sup>, shear wave speed of 100 m/s, and shear attenuation of 0.91 dB/ $\lambda$ . The half-space was overlain by 16 m of water with a sound speed of 1534 m/s and density of 1023 kg/m<sup>3</sup>. A set of 35 traces was generated at each frequency corresponding to the receiver positions relative to a single source located 1 m off the end of the array at a depth of 50 cm. The modeled traces were created using the same wavelets as used to deconvolve the actual data, and the deconvolution was performed exactly as it had been for the actual data. The model simulates the direct arrival as well as the seafloor reflection and waterborne energy that propagates back along the surface and into the sediment, but does not generate scattered arrivals or reflections from sub-seafloor sediment layer boundaries.

The resulting arrival time and magnitude versus distance plots are shown in Fig. 14, analogous to those shown for the ac-

tual data in Fig. 12. At 4 kHz, the pressure magnitude results from the modeled data demonstrate similar separation between shallow and deep receivers as was observed in the actual data, as well as a systematic separation of arrival times not observed in the actual data. No systematic separation in the pressure magnitudes is visible at 10 kHz, whereas the arrival times show separation that appears more dependent on distance than on the receiver depths.

Values of sound speed and attenuation derived from the analysis on the simulated data are shown in Fig. 15. This analysis indicates that at frequencies above 8 kHz the sound-speed ratio may be biased downward by on the order of 0.003, but may be biased upward by as much as 0.03 as frequency is decreased toward 1 kHz. Values of attenuation derived from the deconvolution analysis demonstrate results consistent with the actual attenuation of the model down to frequencies of 8 kHz. From 3 to 8 kHz, the spread of values from the two data subsets captures the trend of the actual attenuation of the model, while below 3 kHz, values of attenuation generated from the deconvolution analysis diverge from the actual attenuation, leveling off in a fashion similar to that observed in the field data. Based on these observations, we conclude that the deconvolution analysis is not able to adequately separate multipath arrivals from direct arrivals at low frequencies. Therefore, we rejected the sound-speed results derived from the deconvolution analysis below 6 kHz and the attenuation results below 3 kHz. This analysis also illustrates that the uncertainties in the attenuation values resulting from interference from other arrivals can be significantly larger than the uncertainties in the least squares fit and in the receiver spacings that are included in the error bars. The error bars shown in the data-model comparisons below were therefore expanded by the difference between the values derived using the entire data set and the values from the data subsets above and below it, shown in Fig. 13.

In an attempt to generate more accurate values of sound speed and attenuation at the lower frequencies, we performed a full waveform inversion of a limited subset of the low-frequency data including all of the data collected when each of the sources

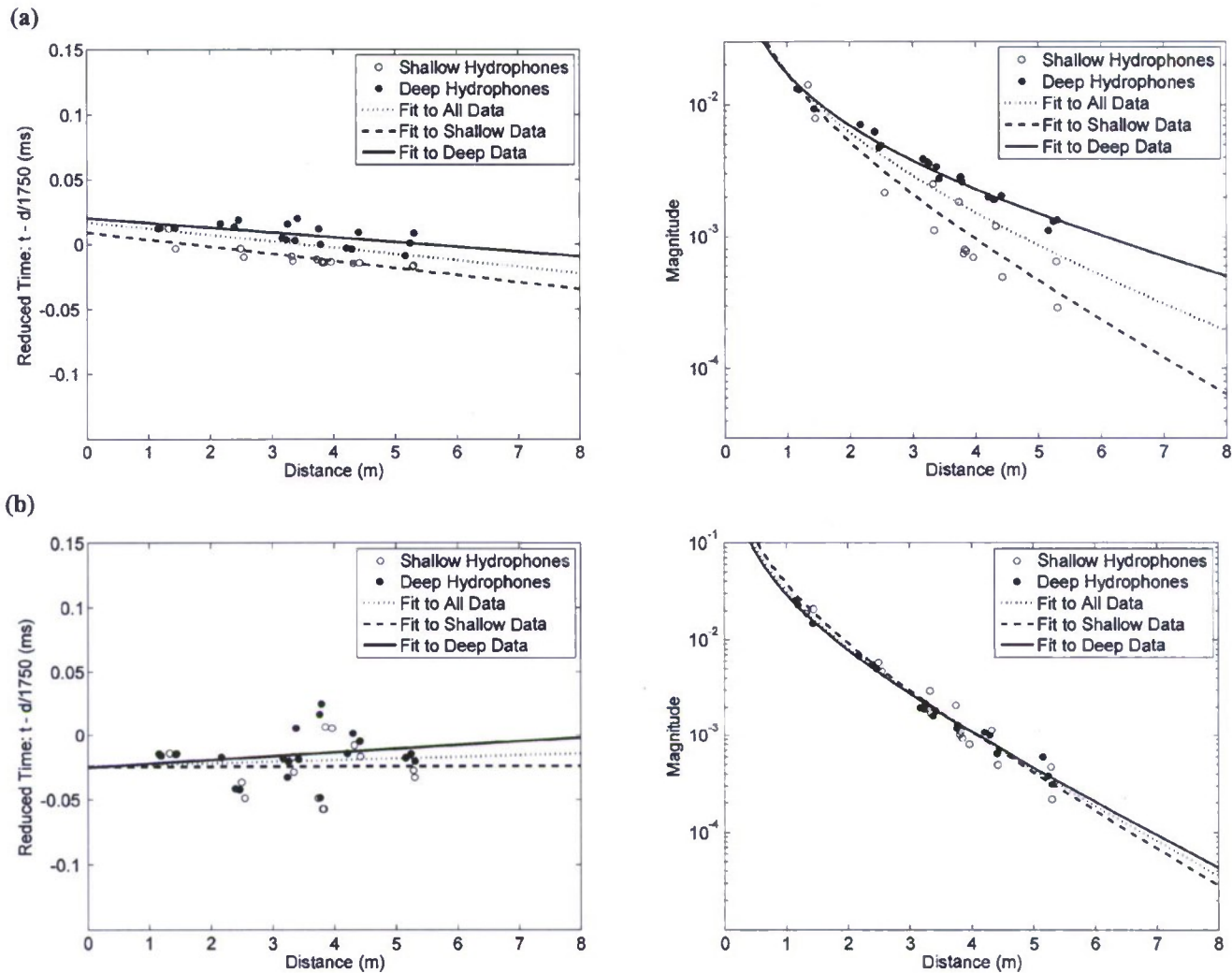


Fig. 14. Reduced arrival times (left) and magnitudes (right) from the deconvolution analysis of the full waveform model data at (a) 4 kHz and (b) 10 kHz.

was located 1 m off the south end of the array at a depth of 50 cm below the seafloor. Simulated full waveform data at each frequency were generated with OASES for an elastic half-space overlain by 16 m of water with a sound speed of 1534 m/s and density of 1023 kg/m<sup>3</sup> for the source–receiver geometry as inverted from the deconvolved arrival times. Simulated data sets were generated with a range of values of acoustic sound speed and attenuation for the half-space, assuming a density of 2051 kg/m<sup>3</sup>, a shear wave speed of 100 m/s, and shear attenuation of 0.91 dB/λ, using the same source wavelets generated from the deconvolution as described above. To invert for the sound speed, the actual data and each simulated data set was windowed to remove later arrivals and each trace was individually scaled to have a standard deviation of 1. All of the traces of each simulated data set were then cross correlated simultaneously with their corresponding traces from the actual data to remove the impact of any constant time offset on the inversion. The peak cross-correlation value was taken as the measure of the goodness of fit of the model to the data. As the sampling of the sound speed was fairly coarse (1–3 m/s) due to the long time required to run each model, the best fitting sound speed was determined

by taking the maximum of a second-order polynomial fit to the peak cross-correlation values within  $\pm 5$  m/s of the maximum value.

The inversion for the attenuation was then performed by generating simulations for a range of values of attenuation, with a 0.1–0.2-dB/λ resolution, with the best fitting sound speed at each frequency as determined from the previous step. The data and simulations were then windowed and all of the traces of the data and of the simulations were scaled simultaneously such that the standard deviation of each data set as a whole at each frequency was equal to 1. The data traces were then all rescaled to have a standard deviation of 1, and the simulated traces were scaled by the same factor as the corresponding trace from the actual data. Without this scaling the inversion is dominated by the traces from the closest hydrophones which have the highest magnitudes. Traces where there was a clear misfit between the simulated and actual data traces, due either to positioning inaccuracy or to the presence of additional multipath arrivals, were removed before inverting for the attenuation. The scaling and time shift of each data set was then varied to find the minimum  $L1$ -norm of the error between each simulated data set and the



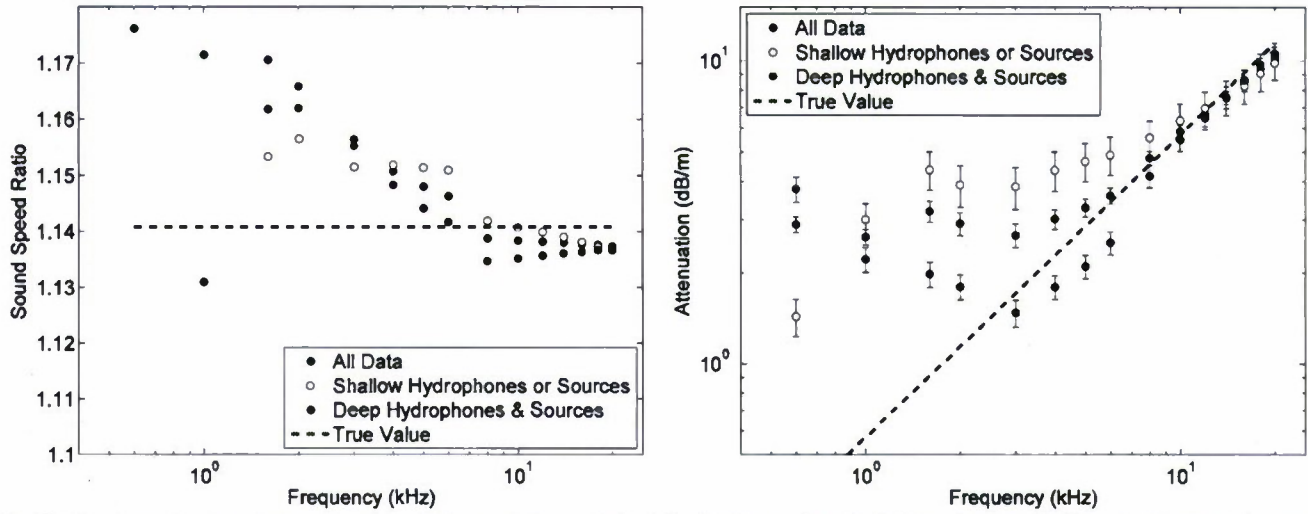


Fig. 15. Sound-speed ratio and attenuation from the deconvolution analysis of simulated traces from the full waveform model. The model inputs were a sound speed of 1750 m/s and attenuation of 1.0 dB/ $\lambda$ . The error bars in the sound-speed ratio plot are not shown as they mostly exceed the limits of the frame due to the small sample size.

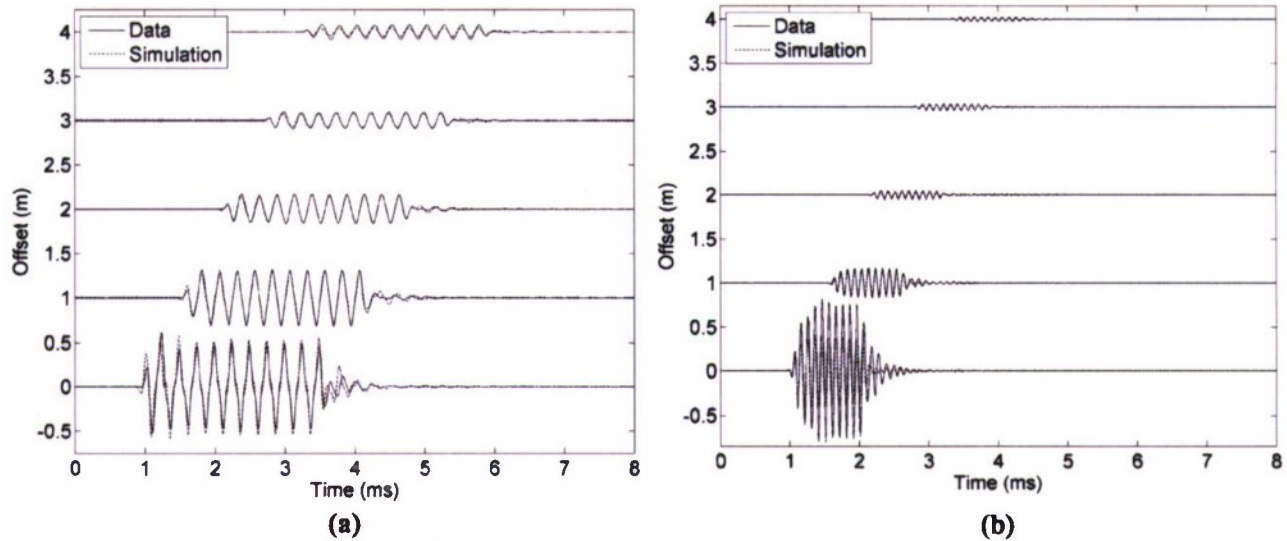


Fig. 16. Comparison of simulated data from the inversion that best matches the actual data at (a) 4 kHz and (b) 10 kHz.

actual data, where the  $L1$ -norm of the errors is the sum of the absolute values of the point-by-point difference between the two data sets. The best fitting attenuation value was taken as the minimum of a second-order polynomial fit to the error values within  $\pm 0.2$  dB/ $\lambda$  of the minimum error value at each frequency.

Fig. 16 shows representative fits between the actual and simulated data traces through the center of the array at frequencies of 4 and 10 kHz. In general, the simulations provide a good match to the actual data when each trace is scaled individually, whereas the amplitudes demonstrate a greater mismatch when the data sets are scaled as a whole. Values of sound-speed ratio and attenuation generated by this analysis are shown in Fig. 17. The values for the two different sources at 6 kHz very nearly overlaid each other. The error bars were generated by performing a bootstrap analysis, where the error bars span the region encompassing 95% of the sound-speed and attenuation values calculated from 1000 bootstrap resamplings of the 35 traces, combined with the uncertainty introduced by the receiver positioning uncertainty (1.2%). Values of sound speed resulting

from this analysis demonstrate an essentially monotonic decrease with decreasing frequency, from a sound-speed ratio of 1.135 above 12 kHz down to a value of approximately 1.115 below 3 kHz. The attenuation values drop from approximately 9 dB/m at the high frequencies down to 1 dB/m below 3 kHz.

### III. RESULTS AND DISCUSSION

Fig. 18 shows the consolidated sound-speed and attenuation results from the core, ISSAMS, and low-frequency array measurements, plotted against frequency. Values of the sound-speed ratio from the higher frequency data sets demonstrate essentially constant sound speeds with frequency above 40 kHz, with individual sound-speed ratio measurements varying from approximately 1.155 to 1.185. The lower frequency data set demonstrates a significant offset from the two higher frequency data sets, possibly partially due to positioning errors in the receiver array. The low frequency values of the sound-speed ratio demonstrate a slight dispersion, dropping from 1.135 to 1.115 as the frequency decreases from 20 to 1 kHz. The

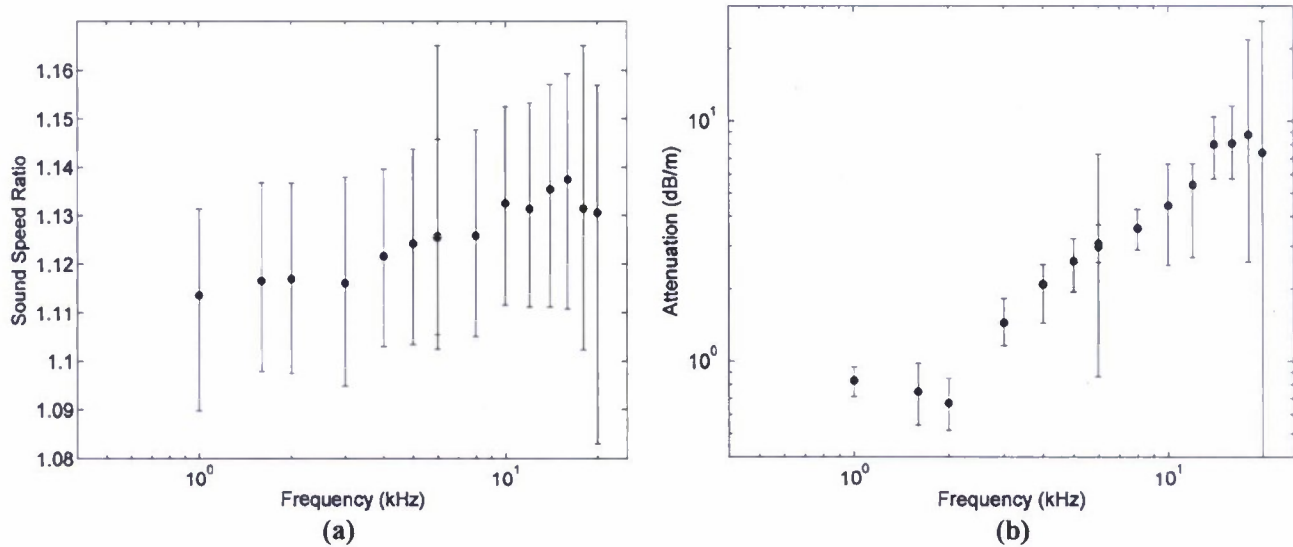


Fig. 17. (a) Sound-speed and (b) attenuation results generated from the full waveform analysis.

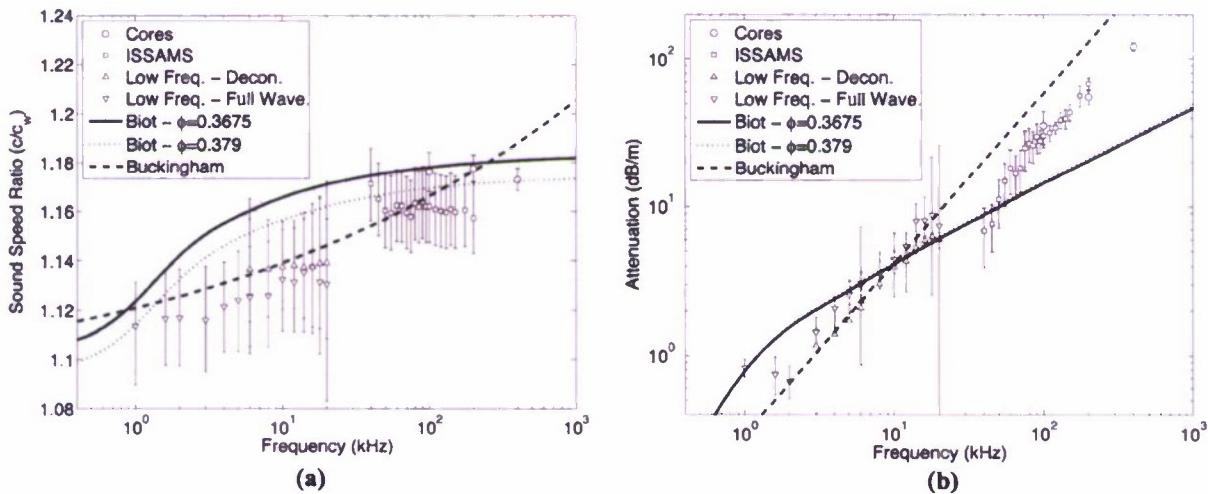


Fig. 18. Consolidated results from all the measurement systems for the (a) sound speed and (b) attenuation. For the ISSAMS and core data the points represent the mean value at each frequency. The Buckingham model line was fit simultaneously to the sound-speed and attenuation data with two free parameters. The dotted Biot model lines were parameterized with values selected in [12] from the range of measurements of sediment and pore-water properties made during SAX04 that best fit their measured speed and attenuation data. The solid Biot model lines used the same set of parameters except the porosity, which was taken as the average value of the porosity measured from the cores collected at the low-frequency site.

attenuation data demonstrate an approximately linear trend over the range of the two higher frequency data sets; from 40 to 200 kHz the average attenuation rises from 7 to 120 dB/m. The low-frequency array data run from approximately 8 dB/m at 20 kHz down to 0.7 dB/m below 2 kHz.

The lines in Fig. 18 show Biot model predictions for and the Buckingham model fit to values of attenuation and sound-speed ratio over the frequency band of the measured data. The dotted lines in Fig. 18 show the Biot model prediction using inputs selected by Hefner *et al.* [12] (shown in Table I), chosen from the range of measurements of sediment and pore-water properties made during SAX04 that best fit their measured speed and attenuation data. The solid lines in Fig. 18 show the Biot prediction using all of the same inputs as for the dotted line except for the porosity, which was taken as the mean value of the porosity measured from the cores collected at the site of the low-frequency array and for which the sound speed and attenuation were mea-

sured in this study. The Buckingham model was fit to the mean data value at each frequency with a nonlinear least squares fit by treating the two uncharacterizable parameters as free parameters, as described in [5] and [6], with the resulting parameters and their 95% confidence intervals given in Table II.

At high frequency, the trends and magnitude of the measured sound-speed ratio are similar to predictions of the Biot model for the higher porosity value. At frequencies from 3 to 20 kHz, the sound-speed dispersion is similar in magnitude to that demonstrated by the Biot trend over the same frequency band, though the magnitude of the high porosity Biot line lies right at the upper limit of the error bars of the data. The fit of the Biot model to the low-frequency data could be improved by varying the input parameters outside the range of the measurements shown in Table I, especially by reducing the permeability value which shifts the transition point to higher frequencies and increases the sound-speed ratio predicted above the transition. The low-fre-



TABLE I  
RANGE OF MEASURED VALUES OF BIOT MODEL INPUT PARAMETERS [12] AND SPECIFIC VALUES INPUT INTO THE MODEL TO DERIVE THE PREDICTIONS SHOWN IN FIG. 18

Biot model parameter	Range of Measured Values	Value Input to Biot model
Porosity	Entire Site: 0.353 to 0.379 Low Freq. Array: 0.353 to 0.378	0.379 0.3675
Permeability	$(1.96 \text{ to } 4.22) \times 10^{-11} \text{ m}^2$	$3.4 \times 10^{-11} \text{ m}^2$
Bulk modulus of sand grains	$(3.2 \text{ to } 4.9) \times 10^{10} \text{ Pa}$	$3.2 \times 10^{10} \text{ Pa}$
Viscosity of water	0.00096 to 0.00099 kg/m·s	0.00096 kg/m·s
Tortuosity of sediment	1.325 to 1.341	1.341
Density of sand grains	2653 to 2660 kg/m <sup>3</sup>	2660 kg/m <sup>3</sup>
Bulk modulus of water	$(2.40 \text{ to } 2.41) \times 10^9 \text{ Pa}$	$2.40 \times 10^9 \text{ Pa}$
Density of water	1023 to 1024 kg/m <sup>3</sup>	1024 kg/m <sup>3</sup>
Shear modulus of sediment frame	$(1.3 \text{ to } 3.0) \times 10^7 \text{ Pa}$	$1.45 \times 10^7 \text{ Pa}$
Bulk modulus of sediment frame		$4.36 \times 10^7 \text{ Pa}$

TABLE II  
INPUT VALUES TO BUCKINGHAM MODEL AND THEIR UNCERTAINTIES BASED ON A NONLINEAR LEAST SQUARES FIT OF THE MODEL TO THE MEAN DATA VALUES AT EACH FREQUENCY

Buckingham model parameter <sup>1</sup>	Value from fit to data	95% confidence interval
Radial stress relaxation exponent, $n$	0.0155	0.0039 to 0.0270
Grain-to-grain interaction factor, $\eta$	0.1762	0.1168 to 0.2356
"Low-frequency sound-speed limit" <sup>2</sup> $c_0$	1663 m/s	1663 to 1736 m/s

<sup>1</sup> Notation from [6]

<sup>2</sup> Calculated from Wood's equation using the inputs shown in Table 1 and held fixed in the fit (not derived from the fit), with the range of values given by the maximum and minimum possible values calculated from the range of values in Table 1.

quency data also follow the trend of the Buckingham model as fit to the data with two free parameters, while at higher frequencies the dispersion predicted by the Buckingham model exceeds that seen in the data, though it does pass within the error bars of practically all of the higher frequency sound-speed data. The high-frequency attenuation data run essentially parallel to, but below, the Buckingham model fit, and demonstrate a significantly steeper trend than the  $f^{0.5}$  trend of the Biot model at those frequencies. The low-frequency attenuation data essentially straddle the two model curves over the entire band from 1 to 20 kHz.

The uncertainties in the values of sound speed and attenuation derived from this analysis do not permit a conclusive test of the validity of the Biot or Buckingham propagation models. Either model could be interpreted to fit the sound-speed measurements over the entire frequency band covered in this study, if parameterized with the upper limit of the measured porosity range. The Biot model, as parameterized with the value of the porosity that was actually measured in cores at the site, consistently overpredicts the mean value of the sound-speed data at all frequencies. The difference between the model predictions for the two different porosity values results from the increased value in the low-frequency limit (i.e., Wood's equation prediction) with lower porosity, a well-established value which is unlikely to be in error. This suggests that the model may overpre-

dict the total dispersion demonstrated by the sediment, possibly a result of the simplified, tube-shaped, porosity geometry assumed by the Biot model. The irregular pore structure of the actual sediment may not permit all of the porosity to contribute to the dispersion mechanisms described by the model. The attenuation values do suggest that the Biot model is insufficient to account for the attenuation at ultrasonic frequencies, where other phenomena, whether scattering or the grain slip mechanisms described by Buckingham's model, must be invoked to produce the higher attenuation observed at these frequencies.

For this study, a primary impediment to being able to test the ability of the Biot and Buckingham models to describe the frequency dependence of the sound speed and attenuation was the interference of multipath signals on the sound-speed and attenuation measurements. In the case of the low-frequency measurements, one method of mitigating these interference effects is to invert for the sediment properties through full waveform modeling of the acoustic signals at each frequency. In this study, the effectiveness of this approach was limited by the inaccuracies in the locations of the array elements, the uncertainty in the source signature once it had been buried in the sediment, and the limited characterization of the sediment below the first 25 cm below the surface. The first two of these issues could be addressed by mounting the majority of the array elements on a rigid frame placed on or above the seafloor, removing the



uncertainties in the array positions and improving the consistency of the source signal. An alternative approach to reducing the multipath interference would be to place the receive elements at greater depths below the seafloor and to suspend the sources in the water column directly above the array and measure the sound speed and attenuation of the signals moving vertically down through the array. The placement of the source in the water column would eliminate the reflection from the seafloor and permit a consistent source signal, while the normal incidence of the source signal on the seafloor would eliminate any multipath through the water column and any refracted arrivals through deeper sediment layers. Vibracores collected at the site of the low-frequency array following the completion of SAX04 show a relatively homogenous sand layer to depths of 4 m, which, in retrospect, would have permitted a receiver emplaced at a depth of 2 m to record two complete cycles at 1 kHz before the arrival of a significant reflected arrival. Higher frequency measurements could be made with a similar, but smaller scale setup.

#### IV. CONCLUSION

We have presented frequency-dependent sound-speed and attenuation measurements made at frequencies ranging from 1 to 20 kHz and from 40 to 400 kHz in the upper 1 m of the seabed near Ft. Walton Beach, FL, using a combination of three different measurement systems. Data from 20–40 kHz was also obtained but contained systematic errors that could not be confidently removed, and so was not included in the final data–model comparison. The sound speed was found to increase from sound-speed ratios of 1.115 to near 1.175 with increasing frequency, demonstrating a dispersion of 0.06 ( $\sim 90$  m/s). The core and ISSAMS data show no dispersion within their individual data sets, whereas the low-frequency data show dispersion in the sound-speed ratio of at least 0.02 ( $\sim 30$  m/s). Thus, most of the overall dispersion is contained in the offsets between the data sets, some of which may be attributed to systematic errors in the separate data sets. The distance between the top of the error bar at the lowest frequency and the bottom of the error bar at the highest frequency does indicate a minimum overall dispersion of at least 0.02 ( $\sim 30$  m/s). The Biot model predicts dispersion of 0.058 in the sound-speed ratio over this frequency band, while the Buckingham model fit to the data shows a dispersion of 0.067. The large uncertainty in the measurements does not allow a clear assessment of the ability of either of these models to fit the measured dispersion in this frequency band.

The attenuation measurements demonstrate an increase from below 1 dB/m below 2 kHz up to values above 120 dB/m at 400 kHz. At frequencies above 40 kHz, the attenuation significantly exceeds the Biot model predictions, but follows an essentially linear trend parallel to the Buckingham model trend, which is fit to the values from the data set as a whole with two free parameters. At lower frequencies, the attenuation straddles the trend demonstrated by the two models. These results suggest that neither model by itself is able to accurately capture the frequency-dependent behavior of the attenuation over the entire frequency band from 1 to 400 kHz.

The principal errors in the lower frequency array measurements result from imprecise positioning of the array elements once embedded in the seafloor as well as from the impact of arrivals other than the direct arrival on the measured sound speed. These arrivals include waterborne signals that travel through the water immediately above the seafloor before propagating back into the seabed and energy reflected off the seafloor or other sediment interfaces below it. These additional arrivals can result in significant uncertainties in the arrival times generated by cross correlation or deconvolution of time series collected at the shallow depths of the measurements presented here. To improve the accuracy of the measurements, we would recommend either placing array elements above the seafloor, simplifying the positioning problem, and using full waveform modeling to reduce the impact of other arrivals, or implanting the receivers at greater depths in the seafloor and positioning the source directly above them to make normal incidence measurements to eliminate arrivals from the waterborne and seabed reflection arrivals.

#### APPENDIX I

##### BOOTSTRAP ANALYSIS FOR ERRORS IN CROSS CORRELATION TIME LAGS

The uncertainties in the time lags generated by the cross correlation of two time series were estimated with a bootstrap analysis adapted from [13]. This analysis was performed by calculating the cross-correlation time lags from 1000 pairs of time series where the individual time samples had been stochastically sampled with replacement. The sampling was done by randomly selecting time samples of a given time series equal to the total number of time samples (thus “with replacement”) such that some samples will be selected multiple times while other samples will not be selected at all. Integer weight factors were applied to each time series where the weight of each time sample was equal to the number of times that sample had been selected. The cross correlation of the two weighted time series was then computed and the time lag determined from the peak value of the cross correlation for each pair. The time lags were calculated from 1000 such stochastically sampled time series pairs to produce a distribution of time lags from which the 95% confidence interval could be determined. Similarly, the 95% confidence interval for the amplitude ratios used to calculate the attenuation are developed by taking the ratio of the rms magnitudes calculated from each pair of weighted time series. The subsequent errors in the sound speeds and attenuations were then calculated using standard error propagation techniques.

As an example, the two simulated time series in Fig. 19(a) consist of identical single cycle sine waves with a period of 128 samples offset by a time lag of eight samples in a 512-sample-long time series. The weights generated for a single iteration of the stochastic sampling for each time series are shown in Fig. 19(b), with some samples selected multiple times and some samples with zero weights such that the sum of all the weights will be 512. The weights are applied to the time series and the time lag is calculated from the cross correlation, shown in Fig. 19(c). After 1000 realizations, the distribution of time lags [Fig. 19(d)] shows an estimate of the uncertainty in the time lag, from which the error bars are developed.



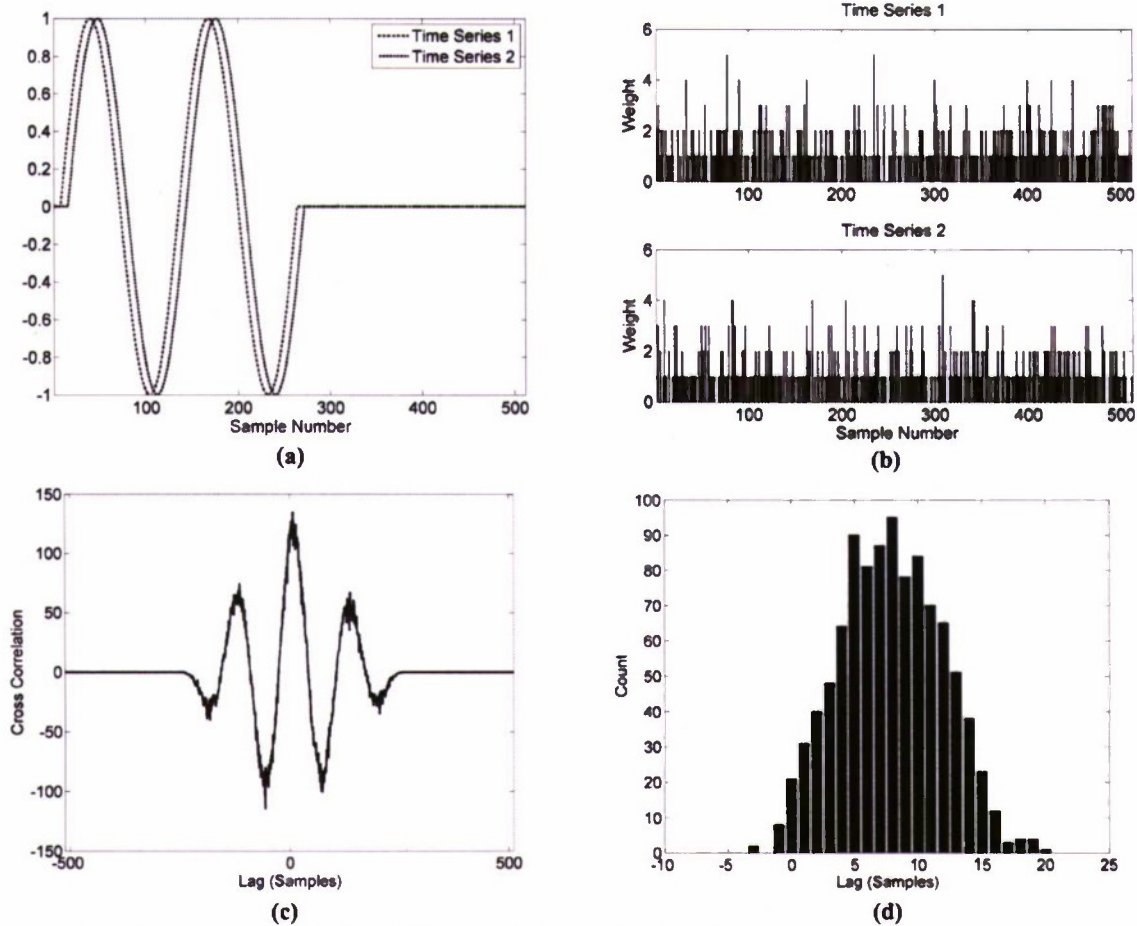


Fig. 19. (a) Two simulated time series with a time lag of eight samples, (b) a pair of stochastically determined weight factors, (c) the resultant cross correlation, and (d) the distribution of time lags generated from 1000 stochastically samples time series used to estimate the uncertainty in the time lag and in sound speed of each measurement.

## APPENDIX II

### SINGULAR VALUE INVERSION FOR LOW-FREQUENCY ARRAY ELEMENT LOCATIONS

The inversion for the positions of the acoustic sources in the low-frequency array was performed by first holding the receiver positions fixed and performing a linearized, iterative, singular value decomposition inversion [14] of the arrival times for the source positions of each of the sources. The inversion consisted of linearizing the time equation

$$t = sd + t_0 = s\sqrt{(X - x)^2 + (Y - y)^2 + (Z - z)^2} + t_0 \quad (6)$$

where  $t$  is the arrival time,  $s$  is the slowness (inverse of speed),  $d$  is the source–receiver distance,  $(X, Y, Z)$  is the source location,  $(x, y, z)$  is the receiver location, and  $t_0$  is the time offset. This equation was linearized by taking the first-order Taylor series expansion in the slowness, offset time, and source location

$$t \approx (s_i d_i + t_0) + \frac{\partial t}{\partial s} \Delta s + \frac{\partial t}{\partial t_0} \Delta t_0 + \frac{\partial t}{\partial X} \Delta X + \frac{\partial t}{\partial Y} \Delta Y + \frac{\partial t}{\partial Z} \Delta Z \quad (7)$$

where  $\Delta s = s_i - s_{i+1}$  is the difference between the current estimate of the slowness and the slowness predicted by the next iteration, with the other differences defined similarly. The resulting set of linear equations for each source–receiver pair was solved

by forming a Jacobian matrix containing the partial derivatives corresponding to the source positions for each source–receiver pair, and inverting it against the arrival time minus the current estimate of the arrival time as shown in (8) at the top of the next page. The inversion was performed with singular value decomposition, where the Jacobian matrix  $J$  was factorized according to

$$J = USV^T \quad (9)$$

where  $U$  and  $V$  are unitary matrices and  $S$  is a diagonal matrix of the singular values. The smallest third of the singular values in each iteration of the inversion were set to zero to limit the change in the poorly constrained vertical positions calculated from the inversion. The inverse was then calculated according to

$$\Delta \vec{v} = VS^{-1}U^T \Delta \vec{t} \quad (10)$$

where  $\Delta \vec{v}$  is the vector of differences, and  $\Delta \vec{t}$  is the vector of arrival times minus the current estimate of the arrival times. The source positions, slowness, and offset time were updated based on the results of the inversion, and the estimated source–receiver distances were recalculated. The inversion was repeated iteratively until the sum of the squares of the change in all of the differences ( $\Delta s$ , etc.) was less than  $10^{-12}$ . The source positions

$$\begin{bmatrix} \Delta s \\ \Delta t_0 \\ \Delta X_1 \\ \Delta Y_1 \\ \Delta Z_1 \\ \vdots \\ \Delta X_{36} \\ \Delta Y_{36} \\ \Delta Z_{36} \end{bmatrix} = \begin{bmatrix} \frac{\partial t_{R1,S1}}{\partial s} & \frac{\partial t_{R1,S1}}{\partial t_0} & \frac{\partial t_{R1,S1}}{\partial X_1} & \frac{\partial t_{R1,S1}}{\partial Y_1} & \frac{\partial t_{R1,S1}}{\partial Z_1} & 0 & \cdots & 0 & 0 & 0 \\ \vdots & \vdots & \vdots & \vdots & \vdots & \vdots & \vdots & \vdots & \vdots & \vdots \\ \frac{\partial t_{R35,S36}}{\partial s} & \frac{\partial t_{R35,S36}}{\partial t_0} & 0 & 0 & 0 & \cdots & 0 & \frac{\partial t_{R35,S36}}{\partial X_{36}} & \frac{\partial t_{R35,S36}}{\partial Y_{36}} & \frac{\partial t_{R35,S36}}{\partial Z_{36}} \end{bmatrix}^{-1} \times \begin{bmatrix} t_{R1,S1} - (sd_{R1,S1} + t_0)_i \\ \vdots \\ t_{R35,S36} - (sd_{R35,S36} + t_0)_i \end{bmatrix} \quad (8)$$

were then held fixed and the same sets of arrival times were used to invert for the receiver positions at each frequency in an analogous fashion as for the source positions.

An error analysis of the resulting source and receiver positions was performed by taking one standard deviation in the arrival times  $\sigma_t$  as the peak width at  $e^{-0.5}$  times the peak height of the Hilbert transform of the deconvolved traces, based on an assumption of a Gaussian-shaped peak. The covariance matrix was then calculated according to

$$\Sigma = VS^{-1}\sigma_t^2(S^{-1})^T V^T \quad (11)$$

where  $V$  and  $S$  are the trailing unitary matrix and the diagonal matrix of singular values from the singular value decomposition of the Jacobian (9) from the first iteration of the inversion. The 95% confidence intervals were taken as twice the square root of the diagonal of this covariance matrix.

#### ACKNOWLEDGMENT

The authors would like to thank C. Kennedy, G. Bower, and R. Mang for their assistance in the preparation of the experimental hardware for this effort, and R. Ray, D. Lott, K. Briggs, and C. Vaughan who provided invaluable diver support deploying experiments and collecting samples. They would also like to thank E. Thorsos and K. Williams of the Applied Physics Laboratory, University of Washington, Seattle, WA, the chief scientist and program coordinators for SAX04, and the captain and crew of the *R/V Seward Johnson*.

#### REFERENCES

- [1] M. A. Biot, "Theory of propagation of elastic waves in a fluid-saturated porous solid. I. low-frequency range," *J. Acoust. Soc. Amer.*, vol. 28, pp. 168–178, Mar. 1956.
- [2] M. A. Biot, "Theory of propagation of elastic waves in a fluid-saturated porous solid. II. High-frequency range," *J. Acoust. Soc. Amer.*, vol. 28, pp. 179–191, Mar. 1956.
- [3] R. D. Stoll, *Sediment Acoustics*. Berlin, Germany: Springer-Verlag, vol. 26, Lecture Notes in Earth Sciences, pp. 149–149.
- [4] M. J. Buckingham, "Wave propagation, stress relaxation, and grain-to-grain shearing in saturated, unconsolidated marine sediments," *J. Acoust. Soc. Amer.*, vol. 108, pp. 2796–2815, Dec. 2000.
- [5] M. J. Buckingham, "Compressional and shear wave properties of marine sediments: Comparisons between theory and data," *J. Acoust. Soc. Amer.*, vol. 117, pp. 137–152, Jan. 2005.
- [6] M. J. Buckingham and M. D. Richardson, "On tone burst measurements of sound speed and attenuation in sandy marine sediments," *IEEE J. Ocean. Eng.*, vol. 27, no. 3, pp. 429–453, Jul. 2002.
- [7] K. L. Williams, D. R. Jackson, E. I. Thorsos, D. Tang, and S. G. Schock, "Comparison of sound speed and attenuation measured in a sandy sediment to predictions based on the Biot theory of porous media," *IEEE J. Ocean. Eng.*, vol. 27, no. 3, pp. 413–428, Jul. 2002.
- [8] N. P. Fofonoff and R. C. Millard Jr., "Algorithms for computation of fundamental properties of seawater," *Unesco Technical Papers in Marine Science*, vol. 44, pp. 46–48, 1983 [Online]. Available: <http://unesdoc.unesco.org/images/0005/000598/059832eb.pdf>
- [9] M. D. Richardson, "Attenuation of shear waves in near surface sediments. In: High-frequency acoustics in shallow water," in *Proc. SACLANCEN Conf., Ser. CP-45*, 1997, pp. 451–457.
- [10] H. Schmidt, "OASES, version 3.1, users guide and reference manual," Dept. Ocean Eng., Massachusetts Inst. Technol., Boston, MA, 2004 [Online]. Available: <http://acoustics.mit.edu/faculty/henrik/oases.pdf>
- [11] K. Aki and P. O. Richards, *Quantitative Seismology: Theory and Methods*, 2nd ed. Sausalito, CA: Univ. Sci. Books, 2002, pp. 119–161.
- [12] B. T. Hefner, D. R. Jackson, K. L. Williams, and E. I. Thorsos, "Mid-to high-frequency acoustic penetration and propagation measurements in a sandy sediment," *IEEE J. Ocean. Eng.*, vol. 34, no. 4, pp. 372–387, Oct. 2010.
- [13] B. M. Peterson, I. Wanders, K. Horne, S. Collier, T. Alexander, S. Kaspi, and D. Maoz, "On uncertainties in cross-correlation lags and the reality of wavelength-dependent continuum lags in active galactic nuclei," *Publ. Astronom. Soc. Pacific*, vol. 11, pp. 660–670, 1998.
- [14] W. H. Press, S. A. Teukolsky, W. T. Vetterling, and B. P. Flannery, *Numerical Recipes: The Art of Scientific Computing*. New York: Cambridge Univ. Press, 2007, pp. 65–75.



**Michael A. Zimmer** received the B.A. degree in geology from Cornell University, Ithaca, NY, in 1996 and the M.S. and Ph.D. degrees in geophysics from Stanford University, Stanford, CA, in 2001 and 2004, respectively.

He spent nearly two years (2004–2005) at the U.S. Naval Research Laboratory, Bay St. Louis, MS, as a National Research Council Postdoctoral Research Associate. He joined ENSCO, Inc., Springfield, VA, in 2005 and is currently a Senior Staff Scientist.

Dr. Zimmer is a member of the Society of Exploration Geophysicists and the American Geophysical Union.





**Leonard Dale Bibee** received the B.A. degree in physics from the University of California San Diego, La Jolla, in 1974 and the Ph.D. degree in earth science from the Scripps Institution of Oceanography, La Jolla, CA, in 1979.

He worked in ocean bottom seismology as an Assistant Professor in Geophysics at the School of Oceanography, Oregon State University, Corvallis, before joining the Naval Ocean Research and Development Activity in 1986. That activity later merged with the Naval Research Laboratory where

he currently works as Head of the Seafloor Sensing Section of the Marine Geosciences Division. His early work studying structure of the seafloor using marine seismic techniques led to studies of interaction of underwater sound with the geology of the seafloor. His interests and work range from sensor development and at-sea data acquisition to signal processing, data inversion, numerical acoustic modeling, and geologic interpretation. Most recently, he has worked with the geoacoustics of marine sediments and the adaptation of existing Navy SONAR for extracting environmental seafloor parameters enabling timely tactical guidance for the fleet.



**Michael D. Richardson** received the B.S. degree in oceanography from the University of Washington, Seattle, in 1967, the M.S. degree in marine science from the College of Williams and Mary, Williamsburg, VA, in 1971, and the Ph.D. degree in oceanography from Oregon State University, Corvallis, in 1976.

He began working at the Naval Ocean Research and Development Activity, now part of the Naval Research Laboratory (NRL), Stennis Space Center, MS, in 1977. Except for a five-year assignment as Prin-

cipal Scientist at the NATO Undersea Research Center (NURC), La Spezia, Italy (1995–1989), he has worked at NRL as a Research Scientist and is currently Head of the Seafloor Sciences Branch in the Marine Geosciences Division. His research interests include the effects of biological and physical processes on sediment structure, behavior, and physical properties near the sediment–water interface. His current research is linked to high-frequency acoustic scattering from and propagation within the seafloor and prediction of mine burial.

Dr. Richardson is a Fellow of the Acoustical Society of America and a member of the American Geophysical Union and Sigma Xi.